Free surface impact on radiation damage in pure nickel by in-situ self-ion irradiation: can it be avoided?

Kan Ma, Brigitte Décamps, Anna Fraczkiewicz, Thomas Jourdan, Frédéric Prima, Marie Loyer-Prost

To cite this version:

Kan Ma, Brigitte Décamps, Anna Fraczkiewicz, Thomas Jourdan, Frédéric Prima, et al.. Free surface impact on radiation damage in pure nickel by in-situ self-ion irradiation: can it be avoided?. Acta Materialia, 2021, 212, pp.116874. 10.1016/j.actamat.2021.116874 . cea-03212396

HAL Id: cea-03212396
https://cea.hal.science/cea-03212396v1

Submitted on 29 Apr 2021

Free surface impact on radiation damage in pure nickel by in-situ self-ion irradiation: can it be avoided?

Kan MA[a,d], Brigitte DÉCAMPS[b], Anna FRACZKIEWICZ[c], Thomas JOURDAN[a], Frédéric PRIMA[d] and Marie LOYER-PROST[a*].

[a]Université Paris-Saclay, CEA, Service de Recherches de Métallurgie Physique, Gif-sur-Yvette, France;

[b]Laboratoire de Physique des 2 infinis Irène Joliot-Curie (IJCLab), Université Paris-Saclay, Orsay, France;

[c]Ecole Nationale Supérieure des Mines de Saint Etienne, Centre Sciences des Matériaux et des Structures (SMS), St Etienne, France ;

[d]PSL Research University, Chimie ParisTech-CNRS, Institut de Recherche de Chimie Paris, Paris, France.

Corresponding author: Marie LOYER-PROST.

Mail: marie.loyer-prost@cea.fr

Courrier: CEA Saclay, DES/ISAS/DMN/SRMP/JANNUS (Bât 126, pièce 58), PC. 162, 91191 Gif-sur-Yvette CEDEX, France.

Telephone +33 (0)1 69 08 24 68.

Abstract

A major issue of in-situ radiation damage studies is related to the influence of free surfaces. Free surfaces in thin foils are indeed strong sinks for radiation-induced defects. Nevertheless, in-situ irradiation is a powerful tool to study real-time microstructural evolution and obtain insight into dynamic mechanisms of radiation damage. Thus, a detailed evaluation of surface effects is essential to validate existing results and provide guideline for future comparative experiments. In this work, nickel is chosen as model material to conduct systematic studies on surface effects due to the high mobility of its self-interstitials. Ultra-high purity Ni thin foils are in-situ irradiated by 2 MeV Ni^{2+} ions at high temperatures (400-700°C). Microstructural evolution analysis and detailed characterization of dislocation loops are performed in function of specimen thickness.

The present work shows: (i) a drastic influence of thickness on the microstructural evolution and irradiated microstructure with the existence of a critical thickness depending on temperature; (ii) a good prediction of an adequate irradiation thickness with a vacancy concentration calculation model; (iii) an impact of free surfaces on the fine distribution of loop Burgers vectors even above the critical thickness; (iv) a first determination of migration energy of vacancies in Ni considering the temperature dependence of the loop-depleted zones; (v) a production bias model showing that a loss of 10% interstitials favors the growth of vacancy loops observed for the first time in Ni at 510°C.

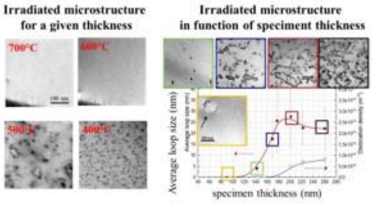

5 keywords

in-situ ion irradiation, influence of surfaces, dislocation loops, vacancy concentration calculations, production bias model

1 Introduction

In-situ transmission electron microscopy (TEM) is a powerful tool to study the real-time microstructural evolution under irradiation and provides reliable details for atomic-scale modeling in order to obtain valuable insight into dynamic mechanisms of cascade damage and defect evolution [1–5]. Despite significant advantages of in-situ irradiations, some issues still remain in the evaluation of the effects of free surfaces in thin foils. Such effects are discussed in some studies in face-centered cubic (fcc) materials (nickel, copper, tungsten and austenitic stainless steels (ASSs)) [4,6–9]. As strong sinks for point defects, free surfaces affect significantly the defect formation and evolution in thin-foil samples. Thus, surface effects need to be fully characterized and understood in each system, which is useful to better understand the fundamental mechanism of radiation damage and to provide an indispensable guideline for comparative experiments.

The irradiation behavior of pure nickel (Ni) and Ni-based alloys as fcc model materials is widely studied to better understand solute effects in fcc structure [10–15]. When irradiated specimens are thin foils, the influence of surfaces in Ni is quite pronounced as reported in the literature [6,14] due to the high mobility of self-interstitials (low migration energy calculated as E^{i}_{m}~0.15eV [16,17]). Nevertheless, surface effects in Ni have still not been unambiguously described. Therefore, it is essential to investigate in detail the irradiation behavior of Ni thin foils and to illustrate unequivocally surface effects as necessary guidance for comparative studies of Ni and its alloys.

In literature, the investigation of the in-situ behavior of pure nickel in thin foils focused mainly on two aspects: (i) the defect evolution under electron irradiation and (ii) the cascade damage produced by ion irradiation.

(i) The first major aspect is the defect evolution under electron irradiation in High Voltage Electronic Microscope (HVEM, voltage generally of 1 MV). Dislocation loops are found to be characteristic in nickel under electron irradiation at low doses [2,18–20]. Most of the observed loops were pure edge faulted Frank loops with Burgers vector **b**=1/3<111> of interstitial nature. Vacancy loops were found only close to a dislocation or on the compression side of interstitial loops [2]. Norris [18], Urban [2], Yoo and Stiegler [19] observed a linear growth of faulted loops over a large range of temperatures. The linear growth rate of Frank loops was found when the temperature exceeds 400°C and was temperature-dependent [2]. The growth of interstitial loops under electron irradiation is explained by the preferential absorption of interstitials by dislocations. The development of a chemical rate theory model with the dislocation bias factor was applied to electron irradiated Ni and allowed a good prediction of defect evolution by several authors [18–23]. Norris interpreted the linear growth of interstitial loops as the case that vacancies are immobile and surfaces dominate all other sinks for interstitials. However, Urban and Wilkens [24] and Kiritani et al. [22] showed that this linear growth at high temperature is actually related to the mobility of vacancies. They found that interstitial loops can grow linearly when the temperature is sufficiently high at which vacancies are mobile. Based on this model, they obtained a good agreement between experiments and simulations of the linear growth rate of interstitial loops in fcc metals and its temperature-dependency.

However, electron irradiations have their own limitations in representing the radiation damage induced by neutrons. Electron bombardments create no cascades which are a characteristic phenomenon of neutron and ion bombardments [25,26]. The defect evolution during electron irradiation takes no account of the influence of cascades that may drastically modify the nature of defects. The data of loop growth rate under ion with the influence of cascades is unavailable in the literature.

(ii) The second aspect is the cascade damage produced by ion irradiation. Results of in-situ ion irradiations in Ni are sparse. The group of Ishino conducted a series of in-situ irradiations using heavy gaseous ions (argon, xenon, and krypton) to study the cascade damage produced during irradiations in Ni [6,27,28]. Their in-situ experiments using 300/400 keV argon ions at 300-773 K showed that clustering of point defects (PDs) was strongly influenced by the presence of point defects sinks: surfaces, pre-existing dislocations, loops and cavities [6]. Wedge-shaped specimens were used to study the effects of surface sinks. It is of great interest to notice two phenomena. Firstly defect-free zones were detected and the thickness of these zones increases with temperature. The second one is the observation of small metastable vacancy defects in thin zones with a very short lifetime during irradiation at 773 K. In thick zones, interstitial loops are formed and grow. These two phenomena show that microstructural evolution depends strongly on the thickness of the specimen, especially at high temperatures indicating a significant influence of surfaces.

The in-situ gaseous ion irradiations of Ishino et al. indeed provide a better understanding of cascade damage created in fcc metals. They point out that the surfaces are strong sinks for mobile PDs and that damage distribution is strongly thickness-dependent [1]. Another group reports that, in Ni, the density of dislocation loop induced by 25 keV He^+ ions irradiated at 400°C increases and then saturates with thickness [29]. However, some important effects are not considered. The fact that they used low energy gaseous ions induces several issues: strong inhomogeneous damage through the thickness, the influence of injected interstitials and influence of gaseous impurities [30–32], which may radically change the defect nature and final microstructure.

In nickel, the data of in-situ high-energy self-ion irradiation including loop growth rate and detailed final microstructure with the influence of surfaces is unavailable in the literature. Moreover, our previous work shows that large independent vacancy Frank loops can be formed in-depth in self-ion irradiated Ni at high temperature [33], which was not reported before. It raises questions on the surface effects on the nature of defects created in heavy-ion irradiated thin-foil Ni since a clear demonstration is unavailable. Besides, a recent in-situ experiment shows that some loops in Ni can glide over long distances under krypton ions (Kr^+) irradiation at 500°C [15]. In iron, mobile loops are depleted in thin-foil samples compared to bulk samples due to image force [34,35]. The experiment [15] may suggest a preferential absorption of mobile loops by surfaces. However, experimental observations are rarely reported in thin-foil Ni in the literature.

To sum up, lack of systematical data on the influence of free surfaces in Ni thin foils under self-ion irradiation raises questions about the representability of irradiated microstructure in thin foils and mechanisms studied from previous in-situ experiments. In recent years, developments in multi-scale modeling and improvements of in-situ techniques are provided. In fcc [36] and bcc [37,38] materials, simulation of long term microstructure under ion irradiation can be performed by rate equation cluster dynamics. High reliability and quantitative in situ experiments are highly desired to validate modeling results for a better understanding of the dynamic mechanisms of radiation damage.

In this study, we describe the first systematical campaign of in-situ high energy self-ion (2 MeV Ni^{2+}) irradiations in thin foils of ultra-high purity nickel to characterize the influence of the free surface to provide guidelines for future experiments and modeling. Microstructural evolution during irradiation is recorded and studied. After irradiations, detailed characterizations of the microstructure, particularly dislocation loops (nature, Burgers vector, size, density and spatial distribution) are performed in function of sample thickness and irradiation temperature. Then, the influence of the free surfaces and dynamic mechanisms of radiation damage are discussed in detail.

2 Method

2.1 Studied materials

Rods of 12 mm diameters of nickel (Ni) were manufactured by cold crucible induction melting at the Ecole des Mines de Saint Etienne (EMSE) in France. The measured impurities content in mass ppm was respectively C<8, S<2, O<3, N<2. 400 µm thick slices are cut from the rod and mechanically polished to 50-80 µm thick. 3 mm diameter foils are punched out and annealed at 1000°C for 2 hours in a vacuum of 10^{-7} mbar followed by air-cooling to reduce the dislocation density. Before annealing, three scans with argon atmosphere are conducted to purify the atmosphere in the furnace and pure zirconium getter is used to absorb residual oxygen during the annealing. Finally, TEM thin foils are prepared by twin-jet electro-polishing in a bath of methanol/nitric acid at -30°C at 10V. In TEM, specimens are clean and hold a good surface state. A low density of dislocations ($<10^{10}$ m^{-2}) is measured by TEM before irradiation.

2.2 Irradiation conditions

Self-ion in-situ irradiations are performed at the JANNUS-Orsay platform Laboratoire de Physique des 2 infinis Irène Joliot-Curie (IJCLab) in France within the framework of the French National network of accelerators for irradiation and analysis of molecules and materials (EMIR&A) [39]. Thin foils are irradiated in a 200 kV FEI Tecnai G2 TEM with 2 MeV Ni^{2+} ions using a rastered beam produced by a 2 Megavolts tandem Van de Graaff accelerator (ARAMIS). The irradiation temperatures are from 400°C to 700°C controlled by a Gatan double-tilt heating holder with an estimated uncertainty of 25°C. The ion flux is 4 ± 0.8 x10^{11} ions.cm^{-2}.s^{-1}. Final fluences are 9 ± 1.8 x10^{13} ions.cm^{-2} and 2.7 ± 0.4 x10^{14} ions.cm^{-2}. Irradiations are performed under a two-beam condition with diffraction vectors type of **g**=<200> or <111> in kinematical bright-field (KBF) mode (s_g>0) [40]. During irradiation, the microstructure evolution is recorded on video and analyzed after irradiation.

The damage profile is calculated by the Stopping Range of Ions in Matter (SRIM) 2013 code [41] using the Kinchin-Pease option with a displacement threshold energy of 40 eV [25,42]. This damage is also calculated by a recently developed molecular dynamic code IRADINA [43] with the same input parameters as SRIM. Calculated profiles are plotted in Appendix A (Fig. A. 1). The two codes are in good agreement for both displacement damage and implantation profile. The thickness of zones of interest is less than 300 nm. Despite a slight variation of dose over the thickness, the final dose in samples is taken at 200 nm thickness and considered as constant and equal to 0.06 dpa for the lower fluence and 0.18 dpa for the higher fluence. The injected interstitials are very few (0.02 ppm/dpa) and can be neglected.

2.3 Defect analysis

From videos, the evolution of dislocation loops during the irradiation is analyzed. Then, irradiation defects are characterized using a 200 kV FEI TECNAI G2 TEM with a LaB_6 filament located in SRMP laboratory in CEA-Saclay. KBF mode is used to optimize the defect contrast.

The size and density of dislocation loops are determined from images under two-beam conditions in kinetic BF mode. The longest distance within the loops is measured manually in ImageJ software and taken as the diameter. Statistic analysis is carried out with an adequate number of loops to calculate their average size. The error bar of the average loop size in figures is the standard deviation. The number density of loops (for short, density of loops in the following) is calculated as the counted number of loops divided by the volume of the analyzed zone. The volume is estimated by multiplying the projected area with the sample thickness estimated by the Convergent Electron Beam Diffraction (CBED) technique [44] along the [220] reflection. The CBED method gives an estimation of the thickness and the extinction distance along the used reflection. Our measurements lead always to an extinction distance of 55 ± 3 nm which is in good agreement with a theoretical value between 57 and 58 nm using jems software [45] (lattice parameter a_0=0.352 nm). The error of thickness measurements is always within 5%. Invisible loops in the zone under each two-beam condition are not contained in the calculated number density. The uncertainty of the density results from the error of the count of loops and the measurement of sample thickness. In our case, the lack of precision in the counted loop number is mainly due to small-size indistinguishable loops and large size agglomerated loops. The error is assumed to be 10%.

The analysis of loop Burgers vectors is performed using the invisibility criterion [41] and a statistic treatment [46] of at least 5 two-beam conditions images along several zone axes. For each **g**, visible loops are counted. A system of equations based on used **g** and corresponding visibility proportion is established and resolved by the least-square method programmed in Scilab software with an error given by the standard deviation from the least-squares.

The inside-outside method [40,47,48] is used under FS/RH convention to determine the nature of pure edge Frank loops with **b**=1/3<111>. As perfect loops with **b**=1/2<110> are not generally pure edge, safe/unsafe conditions are determined for studied loops and the nature of loops under safe conditions is analyzed using inside-outside method [48]. A detailed analysis is presented in Section 3. At last, the depth distribution of loops inside the foil is analyzed by the stereo-imaging technique. A spot of contamination at one surface is taken as a reference point. Two KBF images are taken at the same position before and after tilting beta angle ~17° keeping the same diffraction conditions. The depth of a loop h is calculated by [4]:

$$h = \left| \frac{d_1 cos\theta_2 - d_2 cos\theta_1}{\sin(\theta_1 - \theta_2)} \right|$$

where d_1 and d_2 are respectively the distances between the loop and the rotation axis passing the surface mark point before and after tilting; θ_1 and θ_2 are beta angles before and after tilting. Then, the thickness of the studied zone is equally divided into 5 nm intervals and an analysis of loop frequency distribution along depth is performed. The depth, at which the accumulated frequency reaches 5%, defines the loop-denuded thickness.

3 Results

In this section, the influence of temperature on defect formation is firstly studied for a thickness of around 200 nm as explained in Section 3.1. The maximum temperature where defects are visible is chosen to evaluate the microstructural evolution and loop growth under irradiation. Then, a post-characterization of the irradiated microstructure is performed to investigate the influence of surfaces on dislocation loops. Finally, the thickness-dependency of the irradiated microstructure is presented at lower temperatures to study the role of temperature on surface effects.

3.1 Determination of an adequate irradiation temperature to study surface effects

General microstructures after irradiation in zones of 200 nm thickness are shown by TEM micrographs in Fig. 1 over a large range of temperatures (from 700°C to 400°C). The objective is to find the maximum temperature at which radiation-induced defects can be formed. The frequently used 200 nm thickness for in-situ studies using a conventional 200 kV TEM is chosen for our experiments. The maximum observable thickness of Ni samples in a 200 kV TEM is around 260 nm. If defects can be formed at 200 nm thickness, the thickness marge will be large enough to study the thickness-dependency of the microstructure.

Fig. 1(a-e) present the irradiated microstructure at the same dose (0.06 dpa – 220 s of irradiation) at respectively 700/600/500/450/400°C. At 700°C and 600°C, pre-existing dislocations move during the irradiation but newly-created defects are unstable (appear and vanish). In the literature, dislocation loops have been observed in self-ion irradiated bulk Ni at 575 °C [49] and in He^+ irradiated thin foil Ni up to 700°C at unspecified thickness [29]. The fact that no defect is observed in this work at 600°C and 700°C is very likely attributed to the strong absorption of point defects by surfaces at such thickness.

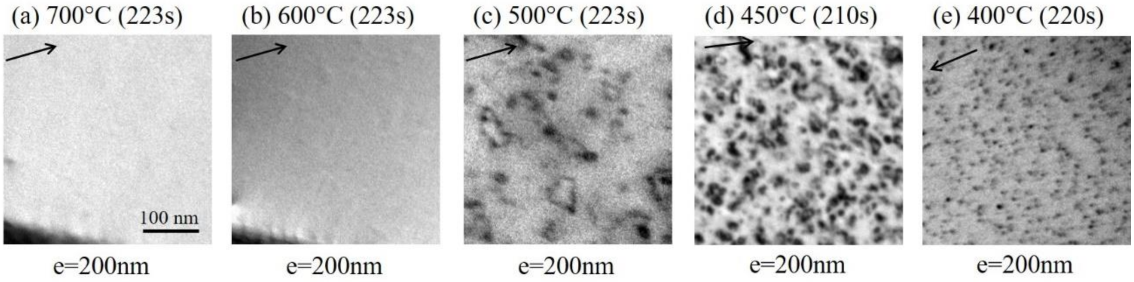

Fig. 1. TEM micrographs showing irradiated microstructures for 200 nm thickness for 220 seconds of irradiation (equivalent to 0.06 dpa) at various temperatures: (a) 700°C, (b) 600°C and (c) 500°C with **g**=<200> close to zone axis <110>; (d) 450°C with **g**=<200> close to zone axis<103>; (d) 400°C with **g**=<111> close to zone axis<110>.

When the temperature is reduced to 500°C, visible dislocation loops are formed under the same diffraction conditions in the same zone irradiated at higher temperatures. Loops grow during the irradiation. The final microstructure at 0.06 dpa (about 220 seconds of irradiation) is shown in Fig. 1(c). Fig. 1(d) and Fig. 1(e) present the final microstructures of two other irradiations at the same dose at respectively 450°C and 400°C. Loops are smaller and show a higher density at lower temperatures. Based on these observations, irradiations around 500°C have been chosen for the next parts of this study.

3.2 Influence of thickness at 510°C on defect formation and evolution (density, size and growth rate)

Fig. 2(a-c) present the microstructural evolution at 510°C at different thicknesses and Fig. 2(d-e) show respectively the evolution of loop density and the average loop size in function of the irradiation duration *t*. Loop densities and average sizes stabilize at different instants for each thickness. At 150 nm thickness, the loop density and average size are approximately constant when $t > 80$ s, so microstructure appears to be in steady-state. At 180 nm and 260 nm, the steady state starts respectively from around 100 s and

130 s. However, the steady state is achieved via different mechanisms. (i) At 150 nm, loops are continuously created during the irradiation. Formed loops grow slightly and most of them quickly disappear, probably to the surfaces. An equilibrium between the loop creation and absorption is established and form a steady-state microstructure. (ii) At 150 nm and 180 nm, the phenomena are similar with larger loop growth at 180 nm. The interaction mechanism of a dislocation loop with the surface is shown in Fig. 2(f): a grown Frank loop is unfaulted into a perfect loop which then immediately glides and disappears. (iii) For a thickness of 260 nm, the microstructural evolution is at first similar to the 180 nm one, but, from 80 s large loops are numerous and tangle with each other, leading to the formation of a dislocation network. Thus, the average size is slightly reduced and finally stabilized.

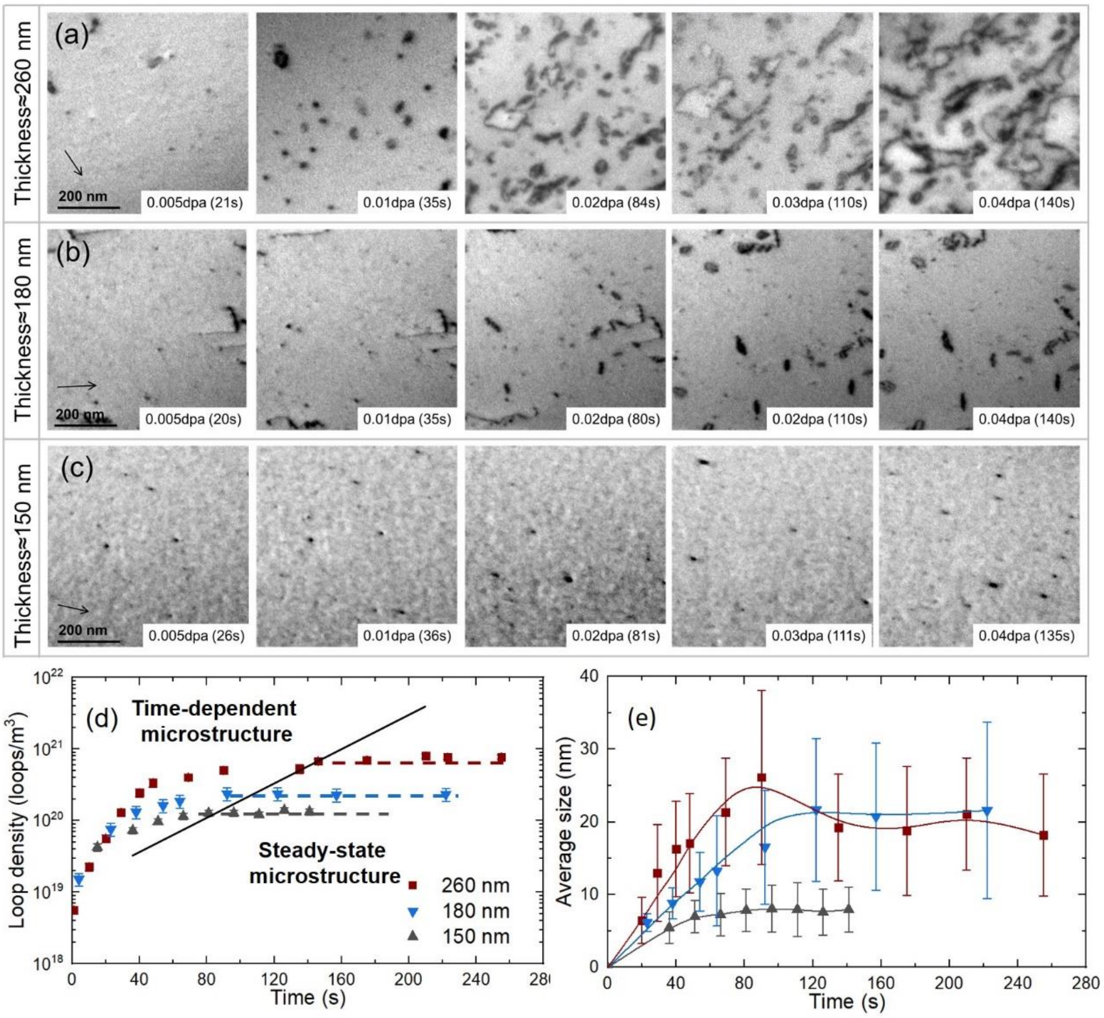

(f) Unfaulting and slip of loop to surface

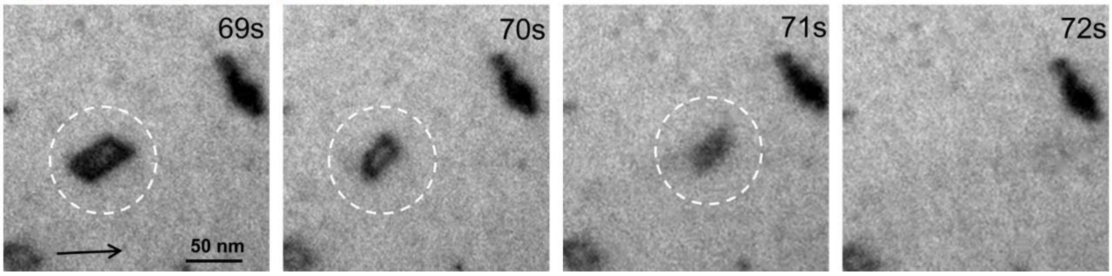

Fig. 2. Microstructural evolution during in-situ irradiation as a function of irradiation thickness and dose at 510°C. (a-c) Selected micrographs illustrating the microstructure recorded under two-beam KBF conditions using (a) **g** = <200>, (b) and (c) **g** = <111>; (d-e) Evolution of loop density and average size in function of irradiation time; (f) unfaulting of a dislocation loop followed by its slip to surface.

Fig. 3(a) presents the typical growth of a Frank loop in function of irradiation time at 510°C. Its growth can be approximately considered as linear with time. A similar phenomenon of interstitial Frank loops was extensively studied under electron irradiation experiments [2,18–20]. This linear growth rate is verified for many other loops, which allows us to calculate an average growth rate for linearly-growing loops. The results are indicated in Fig. 3(b). The loop growth rate increases with thickness as observed intuitively in Fig. 2.

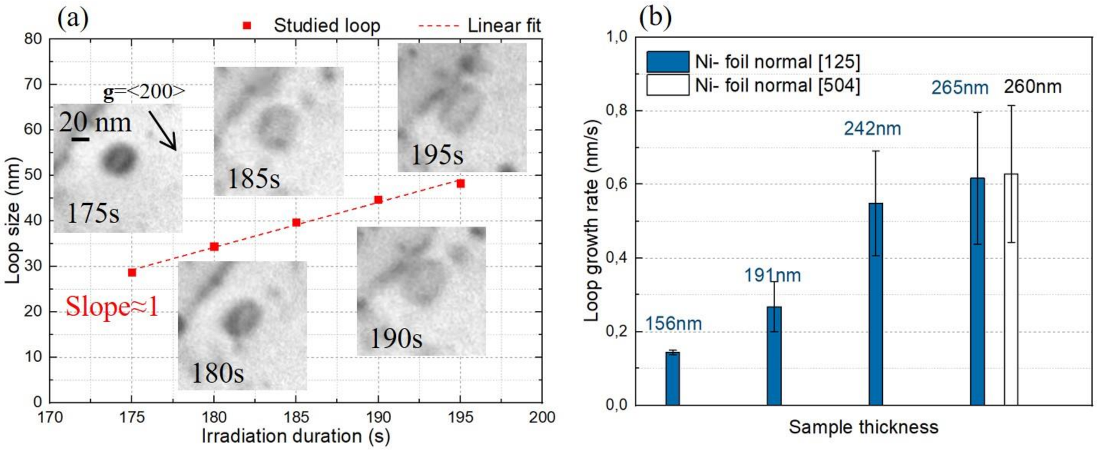

Fig. 3. Determination of loop growth rate during irradiation at 510°C. (a) selected TEM micrographs showing size evolution of a Frank loop in function of time and the corresponding linear fitting; (b) Average loop growth rate in nm/s in function of thickness in two specimens.

It is of great interest to notice that the growth rate is close to saturation taking into account the larger standard deviation when the thickness exceeds 240 nm. Moreover, the same growth rate is observed in another foil with different grain orientations (not shown here). The standard deviation of growth rate is quite important because some loops grow very fast while some grow slowly even in thick zones. This should be attributed to the fact that loops are located at different depths inside the foil where the influence of surfaces changes.

3.3 Post characterization of final microstructure at 510°C (loop average size, density, spatial distribution)

In the following part, we focus on the post-characterization of the final microstructure irradiated up to 0.06 dpa at 510°C. At this dose, the microstructure is in a steady-state and the dislocation network is moderately developed allowing to study numerous individual loops and obtain good statistics.

Loop average size and dislocation line density in function of thickness are presented in Fig. 4(a). The density of loops measured directly from images is plotted by the red curve in Fig. 4(b). In Fig. 4(a), loop average size increases firstly up to a maximum around 190 nm and then decreases and stabilizes to a saturation value. This variation is attributed to the formation of dislocation lines as analyzed above (Fig. 2). During the irradiation, the tangle of large loops contributes to the development of a dislocation network. The formation of such a network reduces the maximum size of loops and therefore their average size.

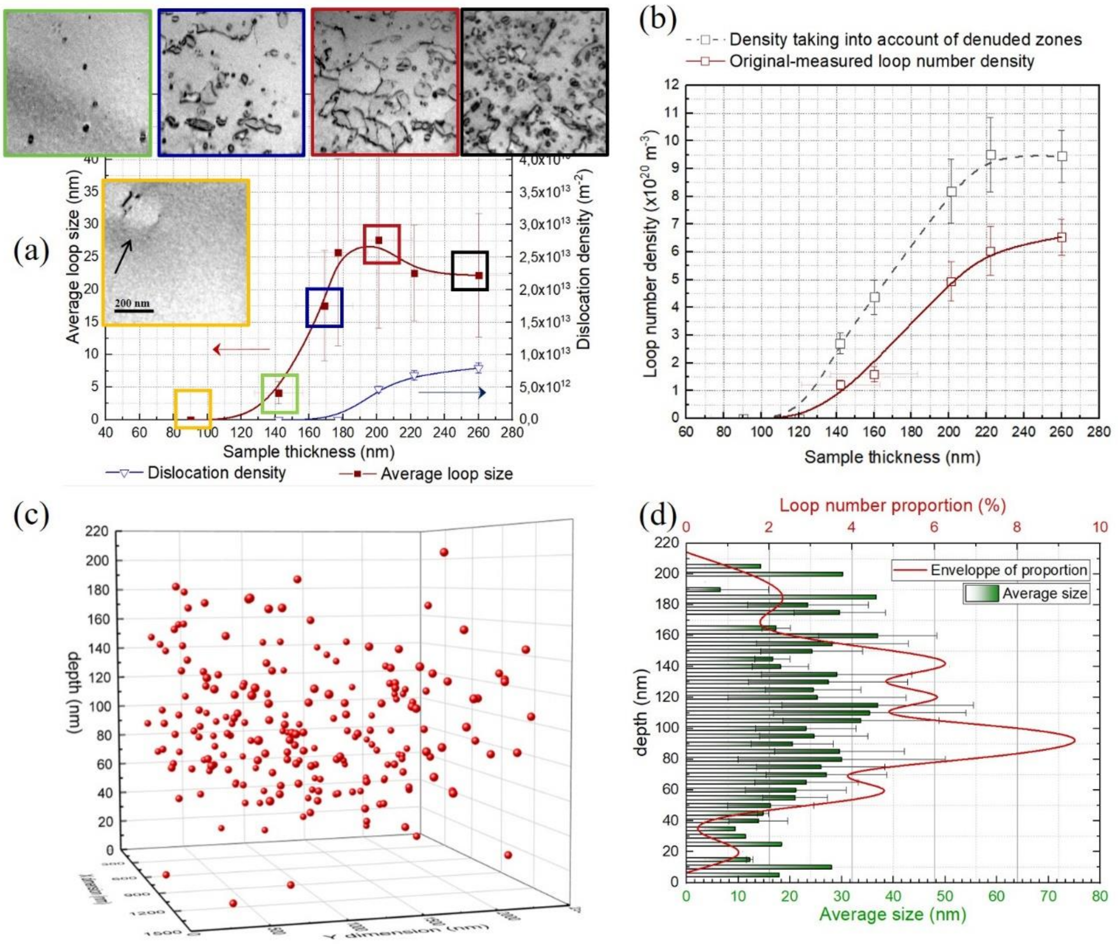

Fig. 4. Final microstructure in function of foil thickness of Ni irradiated up to 0.06 dpa at 510°C: (a) loop density and (b) average size from TEM micrographs taken with **g**=<220>.

Spatial distribution of loops by stereo-imaging technique with (c) 3D visualization of loop position in studied zone of 220 nm thickness and with (d) analysis of loop average size and number proportion v.s. depth, the red curve plotted in Origin using B-spline.

However, in Fig. 4(b), the density of loops (red curve) does not show a saturation even up to 260 nm thickness. Since the calculation of loop number density implicates the total thickness of the specimen, homogeneity of loop spatial distribution may be questioned. The localization of loops is studied using the stereo-imaging technique. Fig. 4(c) shows the 3D distribution at 220 nm thickness. Fig. 4(d) is the average loop size and loop number proportion along the thickness. The number proportion is calculated by dividing the counted number of loops in each layer along depth direction by the total loop number in the studied zone. Loop-depleted zones near surfaces are observed. The strong absorption of near-surface loops by surfaces is accounted for this depletion. The width of loop-depleted zone thickness is approximately 40 ± 5 nm at each side at 220 nm thickness. We choose 5 nm as uncertainty in this work as it is the error of measurement in the stereo-imaging. Furthermore, at 220 nm thickness, loops in the middle of the foil are slightly larger in terms of average size than those close to surfaces.

Taking into account of these loop-depleted zones near surfaces, a corrected loop density using the thickness of loop-located zones is calculated and plotted in the black pointed curve in Fig. 4(b). In this graphical representation, the saturation of loop density is clearly observed. The dependency of these parameters suggests that the final microstructure is thickness-independent above 220 nm. However, it should be noticed that the density shown here takes no account of invisible loops and this is not the real density of existing loops in the sample. Nevertheless, this correction will not change (i) the shape of the black curve in Fig. 4(b) and (ii) the saturation thickness as demonstrated in the next subsection.

3.4 Post characterization of dislocation loops in thick zones (≥ 200 nm) at 510°C (loop type and nature)

In thick zones, Frank loops and perfect loops are both detected. During the irradiation, the absorption of mobile loops by surfaces is observed, which may lead to the depletion of some perfect loops. A loop-type analysis by a statistic method [46] in the 200 nm thickness zone is performed to study the surface effects on loop type. In the first step, microstructure of the same zone is imaged with different **g**. For instance, Fig. 5(a-d) shows four of the seven studied TEM micrographs. According to the authors [46], at least four **g** vectors should be considered (at least two of them non-coplanar) and the accuracy can statistically-speaking be improved with more **g**. In this work, we selected in total seven different **g**, four along the zone axis [001] and three others along [101], which satisfies completely the exigence and provides good accuracy. Then, loop densities are calculated from micrographs taking into account loop-depleted zones (excluding 40 nm for each side). The measured densities are listed in Fig. 5(e).

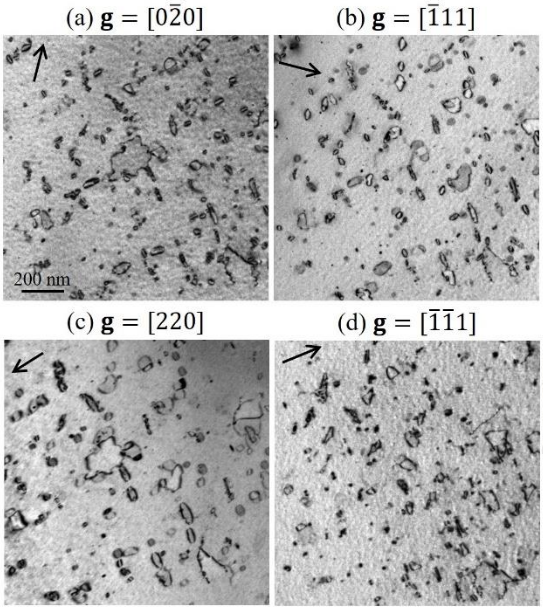

(e)

	Zone axis [001]				Zone axis [101]		
g investigated	020	200	$2\bar{2}0$	220	$\bar{1}\bar{1}1$	$\bar{1}11$	$20\bar{2}$
Loop density ($\mathrm{x}10^{20}\ /\mathrm{m}^3$)	8.0	7.8	6.1	6.1	8.0	6.2	6.0

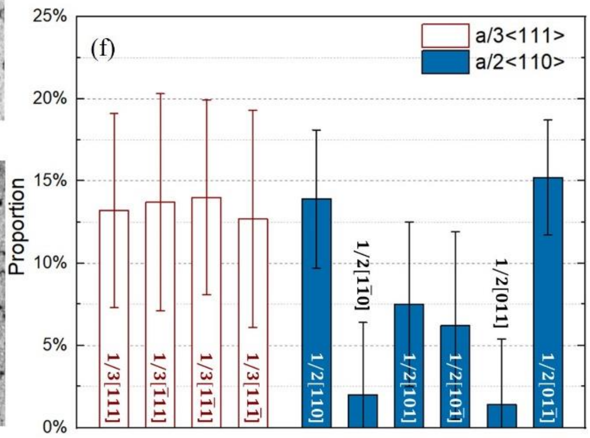

Fig. 5. Loop type analysis by statistic method [46] based on invisibility criterion [41] in Ni irradiated to 0.06 dpa at 510°C: (a-d) TEM micrographs of the same zone showing visibility of loops in function of diffraction vectors **g**; (f) loop number density under seven

different **g** used for statistic analysis; (e) Proportion of each family. Thickness of the zone is around 200 nm and the foil normal is close to [125].

The next step is to establish the system of equations to calculate the density of the aimed loop family. In fcc structure, there are four families of Frank loops and six families of perfect loops. Individual analyses for each family are conducted similarly. The method is illustrated in Equation (1) by the case of the Frank loop family with **b**=1/3[111]. Based on the invisibility criteria, the system of equations for achieved diffraction conditions is:

$$\begin{cases} N_{\boldsymbol{g}=020}^{visible} = \frac{1}{1}N_{\boldsymbol{b}=\frac{1}{3}[111]} + \frac{3}{3}N_{\boldsymbol{b}=\frac{1}{3}<111>/\frac{1}{3}[111]} + \frac{4}{6}N_{\boldsymbol{b}=\frac{1}{2}<110>} \\ N_{\boldsymbol{g}=200}^{visible} = \frac{1}{1}N_{\boldsymbol{b}=\frac{1}{3}[111]} + \frac{3}{3}N_{\boldsymbol{b}=\frac{1}{3}<111>/\frac{1}{3}[111]} + \frac{4}{6}N_{\boldsymbol{b}=\frac{1}{2}<110>} \\ N_{\boldsymbol{g}=2\bar{2}0}^{visible} = \frac{0}{1}N_{\boldsymbol{b}=\frac{1}{3}[111]} + \frac{2}{3}N_{\boldsymbol{b}=\frac{1}{3}<111>/\frac{1}{3}[111]} + \frac{5}{6}N_{\boldsymbol{b}=\frac{1}{2}<110>} \\ N_{\boldsymbol{g}=220}^{visible} = \frac{1}{1}N_{\boldsymbol{b}=\frac{1}{3}[111]} + \frac{1}{3}N_{\boldsymbol{b}=\frac{1}{3}<111>/\frac{1}{3}[111]} + \frac{5}{6}N_{\boldsymbol{b}=\frac{1}{2}<110>} \\ N_{\boldsymbol{g}=\bar{1}\bar{1}1}^{visible} = \frac{1}{1}N_{\boldsymbol{b}=\frac{1}{3}[111]} + \frac{3}{3}N_{\boldsymbol{b}=\frac{1}{3}<111>/\frac{1}{3}[111]} + \frac{3}{6}N_{\boldsymbol{b}=\frac{1}{2}<110>} \\ N_{\boldsymbol{g}=\bar{1}11}^{visible} = \frac{1}{1}N_{\boldsymbol{b}=\frac{1}{3}[111]} + \frac{3}{3}N_{\boldsymbol{b}=\frac{1}{3}<111>/\frac{1}{3}[111]} + \frac{3}{6}N_{\boldsymbol{b}=\frac{1}{2}<110>} \\ N_{\boldsymbol{g}=20\bar{2}}^{visible} = \frac{0}{1}N_{\boldsymbol{b}=\frac{1}{3}[111]} + \frac{2}{3}N_{\boldsymbol{b}=\frac{1}{3}<111>/\frac{1}{3}[111]} + \frac{5}{6}N_{\boldsymbol{b}=\frac{1}{2}<110>} \end{cases} \qquad \text{Equation (1)}$$

Where $N_{\boldsymbol{g}}^{visible}$ is the density of visible loops for the used **g** and summarized in Fig. 5(e), $N_{\boldsymbol{b}=\frac{1}{3}[111]}$ is the density of 1/3[111] Frank loops, $N_{\boldsymbol{b}=\frac{1}{3}<111>/\frac{1}{3}[111]}$ is the sum of three other families of Frank loops, $N_{\boldsymbol{b}=\frac{1}{2}<110>}$ is the sum of six families of perfect loops. This system can be written in the following way:

$$\begin{pmatrix} N_{\boldsymbol{g}=020}^{visible} \\ N_{\boldsymbol{g}=200}^{visible} \\ N_{\boldsymbol{g}=2\bar{2}0}^{visible} \\ N_{\boldsymbol{g}=220}^{visible} \\ N_{\boldsymbol{g}=\bar{1}\bar{1}1}^{visible} \\ N_{\boldsymbol{g}=\bar{1}11}^{visible} \\ N_{\boldsymbol{g}=20\bar{2}}^{visible} \end{pmatrix} = \begin{pmatrix} 8.0 \\ 7.8 \\ 6.1 \\ 6.1 \\ 8.0 \\ 6.2 \\ 6.0 \end{pmatrix} \times 10^{20} = \begin{pmatrix} 1 & 1 & 2/3 \\ 1 & 1 & 2/3 \\ 0 & 2/3 & 5/6 \\ 1 & 1/3 & 5/6 \\ 1 & 1 & 1/2 \\ 1 & 1 & 1/2 \\ 0 & 2/3 & 5/6 \end{pmatrix} \begin{pmatrix} N_{\boldsymbol{b}=\frac{1}{3}[111]} \\ N_{\boldsymbol{b}=\frac{1}{3}<111>/\frac{1}{3}[111]} \\ N_{\boldsymbol{b}=\frac{1}{2}<110>} \end{pmatrix} \text{Equation (2)}$$

This equation is solved by the least-squares method with an error given by the standard deviation from the least-squares. The solution gives the density of three families in Eq.

(2), for instance, $N_{\boldsymbol{b}=\frac{1}{3}[111]}$= 12 ± 5 ×$10^{19}$ m^{-3}. By the same analysis, we calculate the density of other families. Finally, the density of all Frank loop families and perfect loop families is deduced by summing results of each family and are respectively $\mathbf{N_{Frank}}$ = 50 ± 11 ×10^{20} m^{-3} and $\mathbf{N_{perfect}}$ = 43 ± 12 ×10^{20} m^{-3}. Thus the total density taking into account invisible loops is $\mathbf{N_{total}}$ =91 ± 16 ×10^{20} m^{-3} We obtain the proportion of each family by dividing the density of the considered family over the total density. The results are presented in Fig. 5(a). Frank loops are equally distributed among the 4 families with a total density of 50 ± 10 ×10^{20} m^{-3}. The proportion of each Frank loop family is around 13 ± 1% over all loops. On the contrary, a heterogeneous distribution of perfect loops is clearly shown. The family of perfect loops with **b**=1/2$[011]$ shows the lowest proportion and is almost completely depleted while perfect loops with **b**=1/2$[01\bar{1}]$ has the highest proportion, which may be related to the surface absorption and will be discussed in the following section.

With the Burgers vector analysis, a "surface-free" density of loops in the sample (without surface elimination) can be estimated. If we consider that loops are formed equally at the beginning and that the depletion of perfect loops results only from their movement to surfaces, the "surface-free" total density of perfect loops can be estimated by multiplying the highest density by six. The corrected density of perfect loops is 85 ± 20 ×10^{20} m^{-3}. Thus the "surface-free" density of loops taking into account of escaped loops at 200 nm thickness is $N_{total,\ corrected}$ = 135± 22 ×10^{20} m^{-3}. We can also calculate the corrected proportion of Frank loops and perfect loops which is 37% Frank loops and 63% perfect loops. If the loop type analysis is conducted for each thickness, the curve of loop density in Fig. 4(b) can be again corrected. However, we tend to assume that the distribution of Burgers vectors is the same for the studied range of thickness (150-260 nm). With such an assumption, this correction will not change the profile of the curve. So a new curve is not plotted.

In our previous work [33], the relation of the morphology of a Frank loop and its nature was highlighted. For the first time, large Frank loops in Ni irradiated at 450°C were found to be segmented and of vacancy nature. In this study, large segmented loops are observed at 510°C so they must be vacancy-type. The nature of individual loops is determined manually using the inside-outside method [40,47,48] in thick zones (thickness ≥ 200 nm). For tens of characterized loops in each zone, the same vacancy nature for both Frank loops and perfect loops was identified independently on their Burgers vectors. We present here a detailed analysis of two representative loops as shown in Fig. 6.

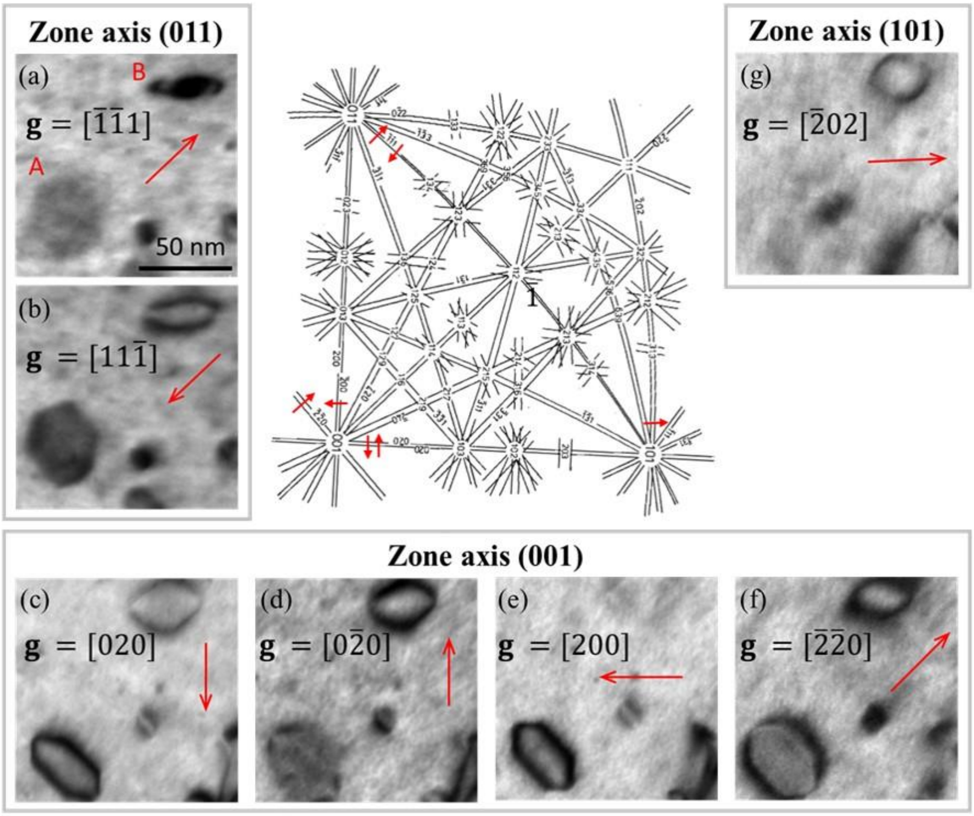

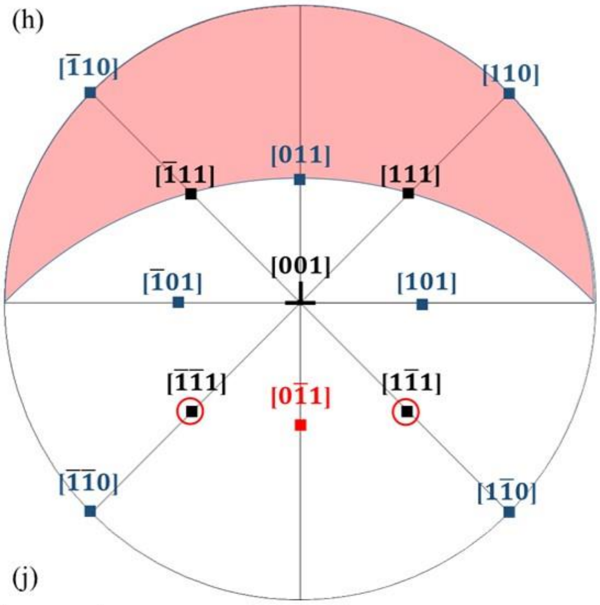

(i)

Application of inside-outside method of pure edge loop	
b	Safe or not
$\pm\frac{1}{2}[011]$	safe
$\pm\frac{1}{2}[01\bar{1}]$	safe
$\pm\frac{1}{2}[101]$	safe
$\pm\frac{1}{2}[10\bar{1}]$	safe
$\pm\frac{1}{2}[110]$	unsafe
$\pm\frac{1}{2}[1\bar{1}0]$	unsafe

(j)

Loop	Contrast of loops (Zone axis [001])			$\mathbf{g}\cdot\mathbf{b}$ for $\mathbf{g}$ (u clockwise)	**b**	Nature
	b direction	$\mathbf{g} = [020]$	$-\mathbf{g} = [0\bar{2}0]$			
A	[111]	inside	outside	<0	$1/3\,[\bar{1}\bar{1}\bar{1}]$	vacancy
B	$[01\bar{1}]$	outside	inside	>0	$1/2\,[01\bar{1}]$	vacancy (**b** in safe condition)

Fig. 6. Determination of Burgers vector and nature of two representative loops in Ni irradiated to 0.06 dpa at 510°C. (a-g) TEM micrographs for analysis of Burgers vectors; Kikuchi map extracted from [40]; (h-i) Stereo-projection along zone axis [001] for

analysis of safe/unsafe conditions [48] for perfect loops $1/2[0\bar{1}1]$, plotted using CaRIne software; (j) determination of loop nature by the inside-outside method [47,48].

Fig. 6(a-g) allow the determination of Burgers vector of loop A and loop B, resulting in **b**=±1/3[111] for loop A and **b**=$1/2[01\bar{1}]$ for loop B. Detailed analysis of b is listed in Appendix B (Table B. 1). Since A is a Frank loop so a pure edge loop, the inside-outside method can be directly applied to determine its nature. Using the FS/RH convention [50] by considering the sense of the dislocation line as clockwise, the inside-outside behavior shown in Fig. 6(c-d) leads to **b**=$1/3[\bar{1}\bar{1}\bar{1}]$ the vacancy nature as shown in Fig. 6(j). The same nature can be deduced from another inside-outside pair in Fig. 6(a-b) as well. For the perfect loop B, we should determine whether it is under safe conditions before applying the inside-outside method [48], as illustrated in Fig. 6(i). Loop B can only be formed from the unfaulting of $1/3[\bar{1}\bar{1}1]$ or $1/3[1\bar{1}1]$ Frank loops by Shockley partials with **b**=1/6<112>. The stereo-projection in Fig. 6(h) shows that these two families of Frank loops are both out of red zones thus in safe conditions according to Fig. 6(i). Therefore, the inside-outside behavior of loop B together with the analysis in Fig. 6(h) confirm its vacancy nature (**b**=$1/2[01\bar{1}]$).

3.5 Role of temperature on surface effects (critical thickness of saturated microstructure) and defect evolution

The temperature-dependency of surface effects shown in Fig. 1 is investigated in detail. Fig. 7(a-b) presents the thickness-dependency of loop number density and average size respectively at 400, 450 and 510°C. The curves of 510°C has been presented in Fig. 3(a) and plotted here to compare with the lower temperatures. Microstructures at 400 and 450°C are shown by TEM micrographs in Fig. 7. At 400°C, loop number density and size are the same at thicknesses of 100 nm and 200 nm. It suggests that saturation of microstructure starts from a thickness lower than 100 nm. At 450°C, the two parameters are lower at 80 nm than at 180 nm and 210 nm. When the thickness exceeds 180 nm, the microstructure is certainly thickness-independent. Based on these observations, a black line is drawn in Fig. 7(a) dividing approximately thickness-dependent zones and thickness-independent zones. In thickness-independent zones, the difference of microstructure is only caused by temperature without any influence of thickness. Microstructural evolutions in saturated zones are recorded at each temperature, as shown in Fig. 7(c-d). The number density at 400°C reaches a steady-state after 120 seconds of irradiation while the average size still increases slowly with time. At 450°C, the steady-state of number density is achieved slightly later than at 400°C. The average size continuously increases with time after the steady state of loop density. However, this steady state of loop density should be “temporary”. Loop density will finally decrease due to the development of a dislocation network. The irradiation at 450°C is conducted for a high dose in the same foil until 680 seconds (equivalent to 0.18 dpa). This tendency is shown by the two points at t=680 s at 450°C in Fig. 7(c-d) where loop size and density are both lower than the values at the so-called steady state.

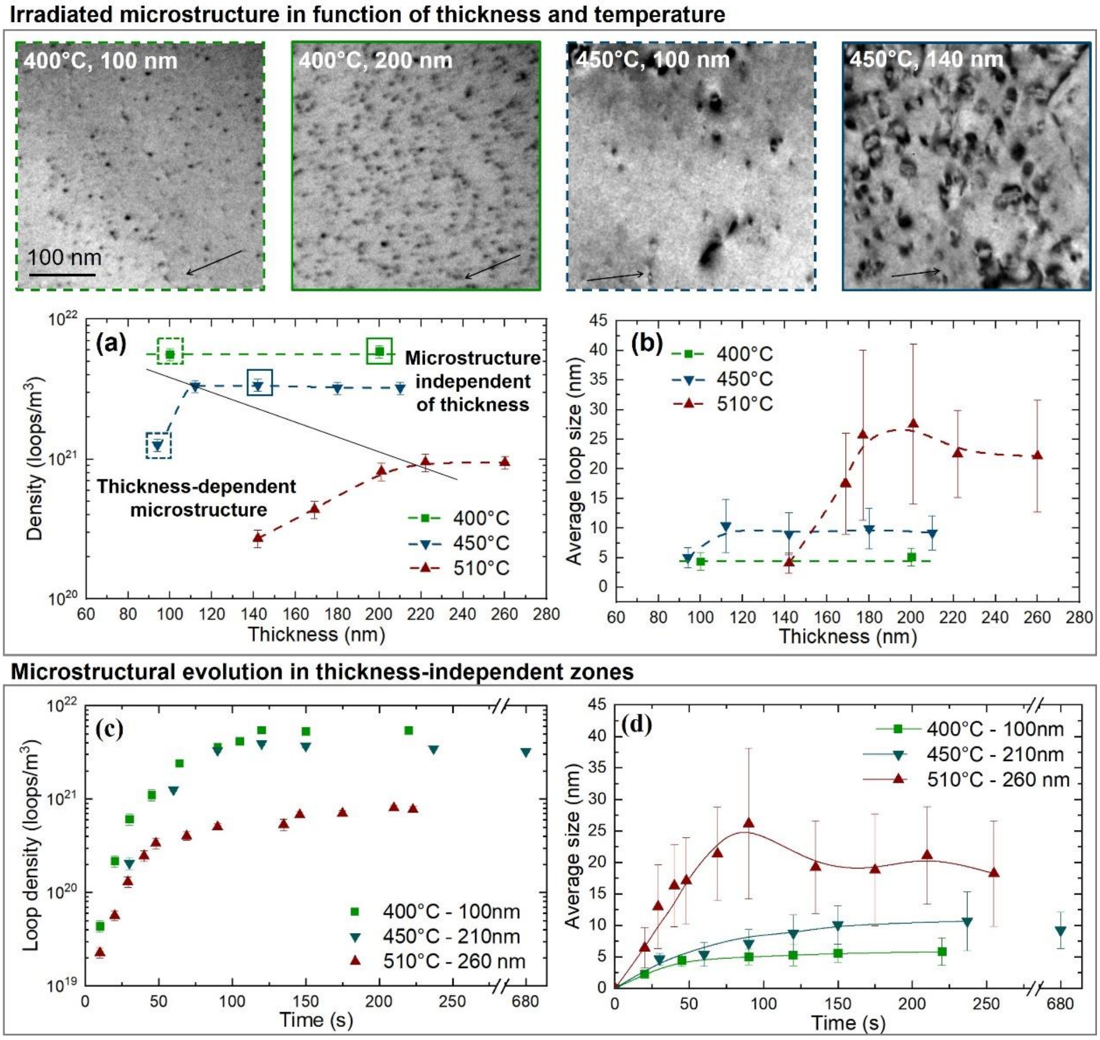

Fig. 7. Influence of surface effects in function of temperature. Evolution of (a) Loop density and (b) average loop size in function of thickness at 400/450/510°C with selected TEM micrographs showing corresponding microstructure; evolution of (c) loop density and (d) average size in function of time in thickness-independent zones at each temperature with selected TEM micrographs showing the real-time microstructural evolution.

The stereo-analysis was also performed at 450°C to study the influence of temperature on the width of loop-depleted zones. Fig. 8 shows the loop-depleted zones in Ni irradiated at 450°C for a 100 nm thickness. Above 100 nm, loop density is too high to correctly identify loops before and after tilting. The width of the zone is about 25 ± 5 nm at each side of the foil.

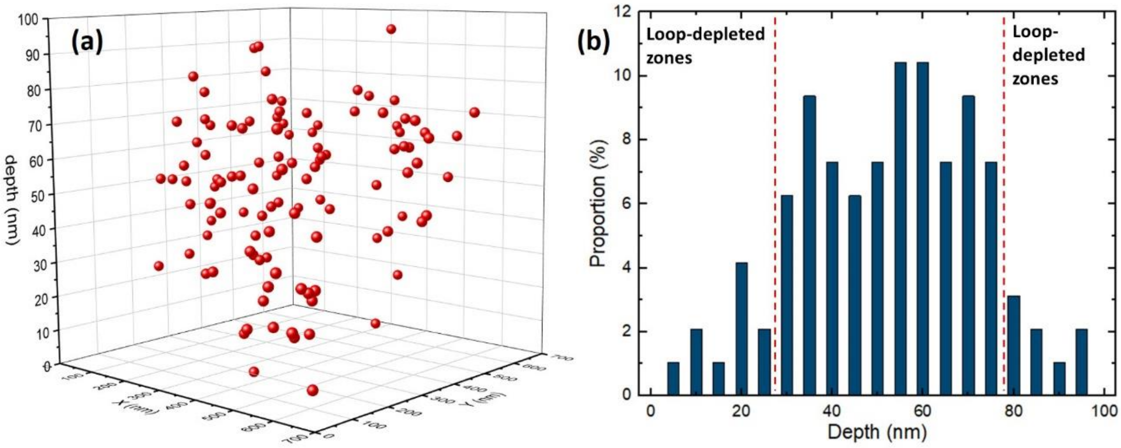

Fig. 8. Loop depth distribution in Ni irradiated at 450°C. (a) 3D visualization of loop position in studied zone of 100 nm thickness; (b) loop number proportion in function of depth by stereo-imaging in Ni irradiated at 450°C showing loop-depleted zones in each side of the foil.

4 Discussion

4.1 Absorption of point defects by surfaces

To evaluate surface effects, the absorption of point defects by surfaces should be considered. We consider here a system without any internal sinks (dislocation lines and loops) to maximize the influence of surfaces. Profiles of the vacancy concentration are calculated numerically by a one-dimensional steady-state rate diffusion equation based on [51] (see details in Appendix C) for the thickness of 50/100/150/180/220/260 nm at 400/450/500/600°C. Based on this numerical solution, we can calculate the normalized profile (Y/Y_{max} for each thickness) and the profile of the concentration of vacancies ($C_v = YC_{v,\infty}$). The results are presented in Fig. 9(a-h).

For a given temperature, for instance 510°C (see Fig. 9(b) and Fig. 9(f)), the profile expands from a typical surface-dominated one to a recombination-dominated one with increasing thickness. This could explain the thickness-dependency of the irradiated microstructure shown in Fig. 4(a) and Fig. 4(b). At 510°C, a recombination-dominated zone occurs in the center of the foil when t=150 nm. It corresponds to the beginning of loop growth in thick zones experimentally observed. Obviously, the fraction of volume which is less affected by surface increases with thickness. Finally, in thick zones (220 nm), the vacancy concentration is stabilized and reaches a thickness-independent stable value, which could lead to the observed thickness-independent microstructure. The same tendency is shown at lower temperatures. However, surface effects remain strong at 600°C in the studied thickness range. When the temperature decreases, the profile expands more quickly with increasing thickness from surface-dominated profiles to recombination ones. This could be related to the temperature dependency of critical thickness for saturated microstructure.

For further quantitative evaluation of the absorption by surface, the ratio of vacancy flux to surface $J_{v,surf}$ and to the recombination $J_{v,recomb}$ is calculated and shown in Fig. 9(i). The lower dashed line corresponds to a ratio of 0.01 i.e. approximately 1% of PDs are absorbed by surfaces. The corresponding thicknesses for each temperature are 80/120/190 nm respectively for 400/450/510°C. Considering the simplicity of the model without effects of internal sinks (radiation-induced loops during the irradiation and thermal vacancies as recombination site [51]), this estimation is fairly in good agreement with our experiment observations (80/110/220 nm) in Fig. 7(a). The upper dashed line in Fig. 9(i) corresponds to 90% absorption of PDs by surfaces. It is worth noting that the results in Fig. 9(i) is for the very center of the foil, where the surface absorption is the lowest across the entire depth. The surface absorption in the rest volume is higher than 90%. Thus, it suggests a critical thickness under which the sample will be completely free of defects. It reads respectively 18/25/40/70 nm for 400/450/510/600°C. This is in fairly good agreement with our observations at 510°C (under 40 nm thickness, no loop is observed) and with those reported by other authors at lower temperatures (~20 nm at

400°C in Ni under Ar^+ irradiation [1]). However, the critical thickness for the defect-free zone is usually larger than the calculated one because other factors should be taken into account, such as absorption of formed defects by surfaces.

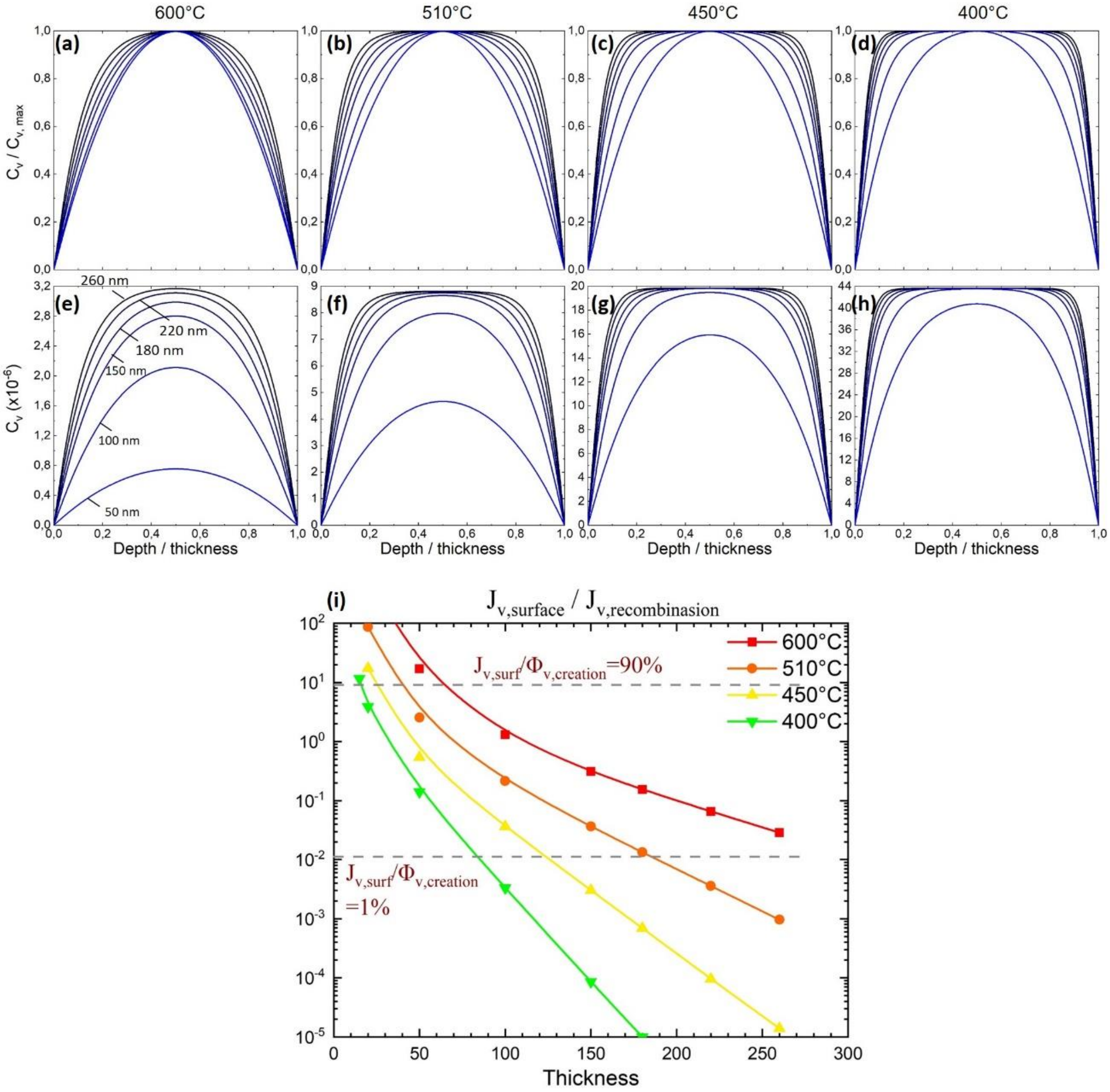

Fig. 9 Profiles of (a-d) normalized and real (e-f) vacancy concentrations and (i) ratio of vacancy flux towards surfaces and to recombination in the center of the foil in function of thickness (50/100/150/180/220/260 nm) and temperature: concentration profiles at (a,e) 600°C; (b,d) 510°C; (c,g) 450°C; (d,h) 400°C; in (i), the upper dashed line corresponding to 90% absorption of PDs by surfaces and lower dashed line corresponding to 1% absorption by surfaces.

4.2 Surface denuded zones

The depth distribution of radiation-induced defects in thin foils has been investigated in several materials [1,4,19,38,52,53] to better describe irradiated microstructures and understand the mechanism of the defect formation. In the literature, the thickness of depleted zones was found to be about 12 nm at 300°C and 20 nm at 400°C in Ni under Ar^+ irradiation [1] for each side of the foil. Another experiment showed that no loops were detected at the irradiation entry side until 50 nm in Ni irradiated by 25 keV He^+ at 550°C [29]. In electron-irradiated Ni, the depth profile of the interstitial loop size was studied in a 450 nm thick foil at 450°C [19]. All studied loops were located at least 30 nm from the closest surface. In the present work, a loop-depleted zone is indeed shown in Fig. 4(d) and is roughly 40 nm wide from each foil surface in self-ion irradiated Ni at 510°C. Although the amount of data is limited and irradiation conditions are different, these data at least are in reasonable agreement and suggest that the width of surface denuded zones depend on temperature. The width of surface denuded zones L was described by a formula of Foreman [51]:

$$L = \sqrt{\frac{D_v C_{v,\infty}}{G}} = \left(\frac{D_v}{G K_r}\right)^{\frac{1}{4}} \qquad \text{Equation (3)}$$

where G the PD production rate and K_r the recombination coefficient are constant. L is thus proportional to $D_v^{\frac{1}{4}}$ so proportional to $\exp(-E_{v,m}/(4k_BT))$. Experimental results of ln(L) (L=12/20/25/40/50 nm) in function of $(4k_BT)^{-1}$ for 400/450/510/550°C are plotted in Fig. 10. Error bars are plotted only for our experiment data since the uncertainty of L is not given in the literature. Data at T≥400°C leads to a fairly good linear fitting considering the error bar. The fitted slope reads 1.2 ± 0.1 eV, which gives a good estimation of migration energy of vacancy from self-diffusion experiments (1.24 eV [17]) and by some simulations (1.32 eV [15], 0.92-1.46 eV [54]) in the literature.

Yet, the data at 300°C deviates from the fitting line. There are three possible explanations. The first explanation is related to the uncertainty of the loop-denuded thickness determination. The uncertainty and the error bar increase significantly at lower temperatures. The fact that error bars were not given at 300°C and 400°C in [1] and at 550°C in [29] could induce a slight discrepancy of the plotted slope. The second reason might be a potential influence of injected gaseous impurities (Ar^+ irradiations at 300/400°C in [1]) on the mobility of vacancies since it is known that impurities can impact the migration of PDs [55]. The third one is the applicability of Equation (3) at low temperatures. At $T<400°C$, the nature of loops nucleated at 300°C could change. Foreman suggested that the denuded zone of interstitial defects should be a measure of the interstitial mobility instead of the vacancy mobility [51]. Therefore, the correlation between $\ln(L)$ and $(4k_BT)^{-1}$ might no longer be related to the diffusion coefficient of vacancies but the one of interstitials. This will lead to a much smaller slope (E^i_m~0.15eV [16,17]), which consists with the reduction of slope towards lower temperatures shown in Fig. 10.

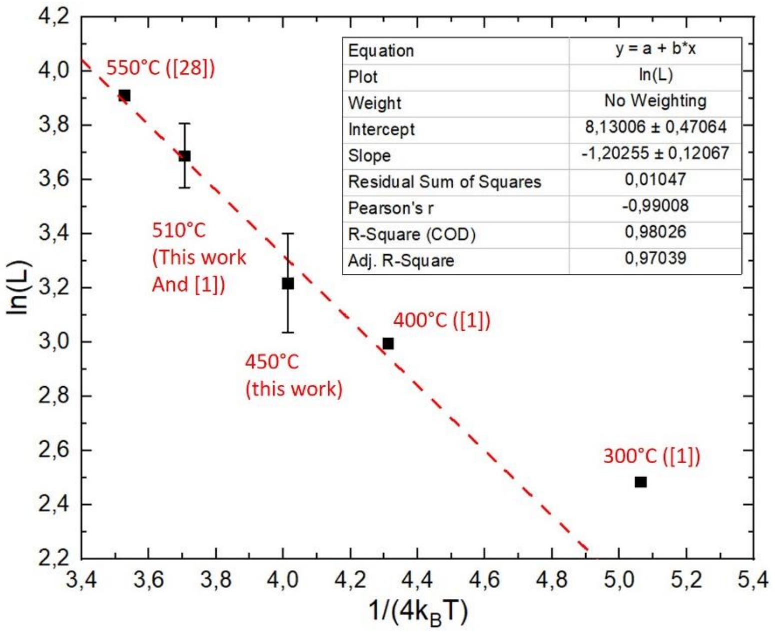

Equation	y = a + b*x
Plot	ln(L)
Weight	No Weighting
Intercept	8,13006 ± 0,47064
Slope	-1,20255 ± 0,12067
Residual Sum of Squares	0,01047
Pearson's r	-0,99008
R-Square (COD)	0,98026
Adj. R-Square	0,97039

Fig. 10. Correlation between the width of loop-depleted zones and temperatures. Linear fitting is performed using the data at 550/510/450°C. The error bar of data in this work results from the uncertainty of the 5 nm thickness of depleted zone.

4.3 Surface effects on loop type

In Fig. 5(e), unequal distribution of Burgers vectors of perfect loops is observed in irradiated Ni. To explain this phenomenon, two mechanisms should be considered: (i) a preferential absorption of some loops by surfaces and (ii) a preferential formation of perfect loops with some specific Burgers vectors.

The first one is very likely involved since many loops are indeed found to move straight and then disappear probably at surfaces as shown in Fig. 2(f). Fig. 11(a) shows the straight movement of three additional loops at 510°C. These TEM micrographs were taken along zone axis <013> with **g**=<200> during the irradiation. This quick straight movement is very likely the slip. To analyze the direction of their movement, stereo-projection along [013] is shown in Fig. 11(b). The motion takes place always along <110> directions. It is in agreement with the fact that slip of perfect dislocation in fcc materials occurs on {111} planes in <110> directions [56].

It is interesting to wonder whether loops slip along the direction of their Burgers vector. It is difficult to analyze the Burgers vector and their habit plane during the irradiation. Thus, a post-characterization is performed in irradiated Ni (510°C/0.06 dpa) to study the Burgers vector and habit plane of loops. Fig. 12 shows a typical rhombus-shape perfect loop (no fault contrast inside the loop). Its Burgers vector is 1/2$[01\bar{1}]$ (Fig. 12(b-c)). The two segments of the rhombus (D1 and D2) are [321] and $[\bar{3}21]$. The loop plane normal n_{loop} is obtained by $n_{loop}=[321]\times[\bar{3}21]=[0\bar{1}2]$ (conventionally n_{loop} pointing always upward). Perfect loops with similar segment directions and loop planes were detected in Al-based alloys in the literature [57]. Fig. 12(d) shows schematically the loop structure. The two segments [321] and $[\bar{3}21]$ are respectively in $(\bar{1}11)$ and (111) planes which are slip planes in fcc structure. The common slip direction on these planes is $[01\bar{1}]$ which is collinear with the Burgers vector of the loop. Moreover, the exact habit plane and the Burgers vector give an unambiguous determination of its nature which is vacancy-type since $\mathbf{n}_{loop}\,.\,\mathbf{b}<0$ [48].

Here we tend to assume that the motion of perfect loops follows their Burgers vector. To understand the unequal distribution of perfect loops in post-characterization (Fig. 2(f)), the foil normal and different Burgers vectors of perfect loops are plotted in Fig. 11(c). The angle between the foil normal and each Burgers vector is shown. The [011] direction has the smallest angle with the foil normal while $[01\bar{1}]$ and [110] are far from this direction. We could expect that loops having shorter path lengths along the motion direction to the foil surface are more readily to be lost than loops of other Burgers vectors. This is in agreement with the experimental observations of most families except 1/2$[\bar{1}10]$ perfect loops. It may be understood geometrically as the $[\bar{1}10]$ direction is almost parallel to the surface (see Fig. 11(c)). If perfect loops tend to rotate their loop habit plane to become edge loops i.e. Burgers vector perpendicular to loop plane, the habit plane of 1/2[$\bar{1}$10] loops will be almost perpendicular to the surface. The interception of 1/2[$\bar{1}$10] loops with surfaces is the geometrically easiest. The interception results in the absorption of loops by surfaces and finally leads to a depletion of this family. It is worth noting that such an influence of surfaces remains strong at such a thick zone where the absorption of PDs by surfaces is moderate. It shows that surface effects are significant not only on the scale of primary defects (like PDs) but also on the scale of larger defects (like dislocation loops).

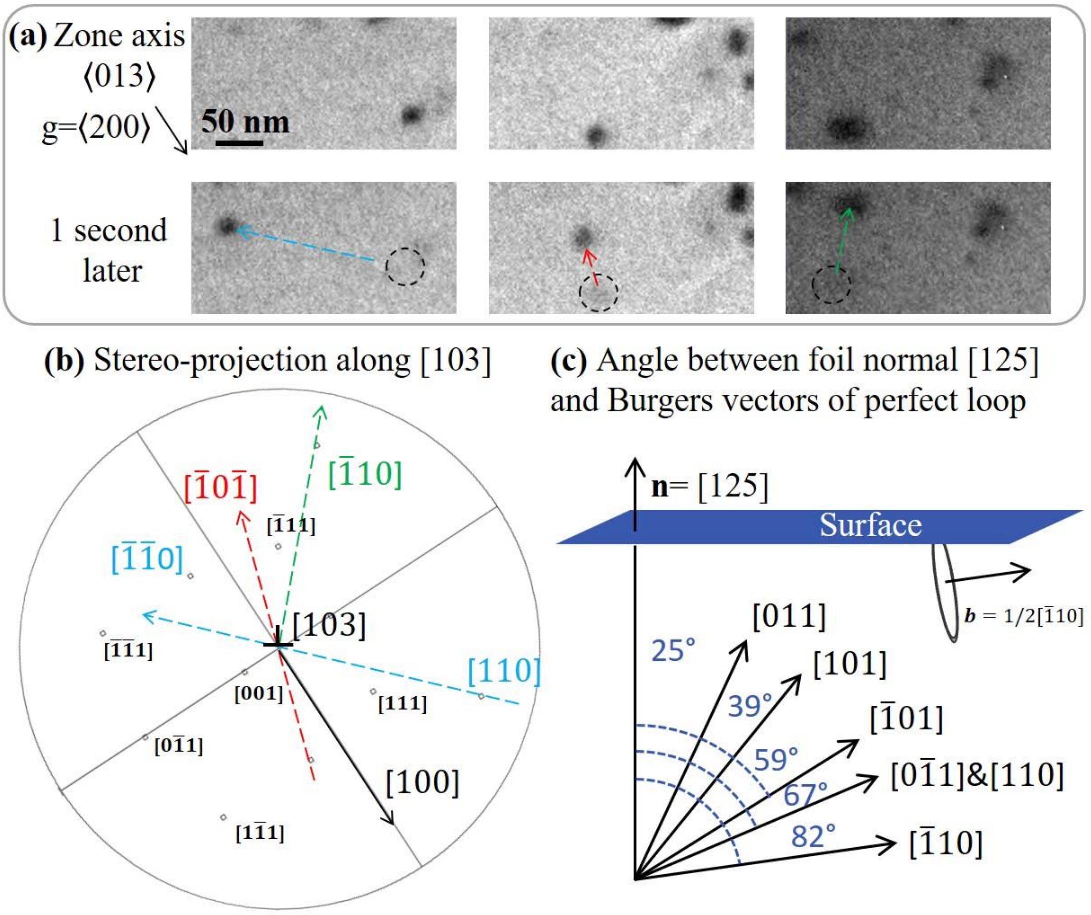

Fig. 11. Analysis of motion direction of dislocation loops in irradiated Ni at 510°C. (a) TEM micrographs showing the movement of three loops with the motion direction indicated by dashed arrows; images taken along zone axis <013> with g=<200>; (b) stereo-projection along [013] with motion directions indicated; (c) angles between the foil normal [125] and Burgers vectors of perfect loops.

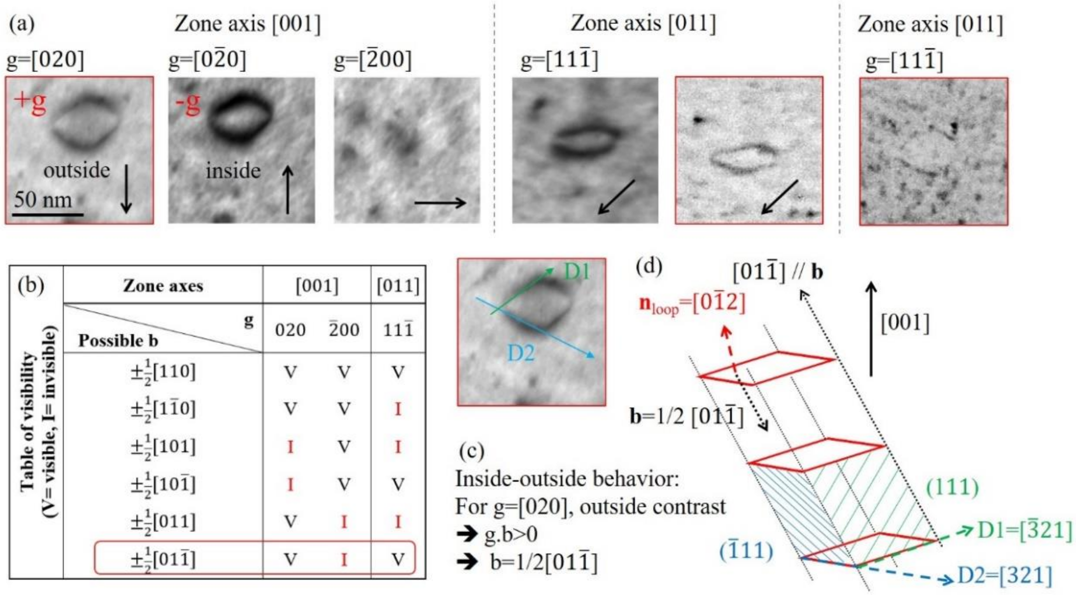

(b) Table of visibility (V= visible, I= invisible)	Zone axes	[001]		[011]
	Possible b \ g	020	$\bar{2}$00	11$\bar{1}$
	$\pm\frac{1}{2}$[110]	V	V	V
	$\pm\frac{1}{2}$[1$\bar{1}$0]	V	V	I
	$\pm\frac{1}{2}$[101]	I	V	I
	$\pm\frac{1}{2}$[10$\bar{1}$]	I	V	V
	$\pm\frac{1}{2}$[011]	V	I	I
	$\pm\frac{1}{2}$[01$\bar{1}$]	V	I	V

Fig. 12 Analysis of Burgers vector and habit plane of a rhombus perfect loop in Ni irradiated at 510°C up to 0.06 dpa. (a) TEM micrographs showing the visibility of the loop with the same scale bar in the first one. (b) Table of visibility showing the Burgers vector. (c) Inside-outside contrast analysis determining the sign of the Burgers vector. (d) Directions of line segments and the habit plane of the rhombus loop; the segment directions are determined from TEM micrographs with red frame.

4.4 Growth of vacancy loops in Ni at high temperatures

This work shows that dislocation loops formed in Ni at 510°C under irradiation are vacancy-type and segmented. This observation is in perfect agreement with our previous study that showed for the first time a strong correlation between the morphology of Frank loops and their nature: interstitial Frank loops are non-segmented while vacancy ones are segmented [33]. During the in-situ experiments at 510°C, Frank loops (such as the one in Fig. 2(f)) are segmented. Therefore, the dislocation loops that grow under irradiation (Fig. 2(a-c)) should be vacancy-type. Our characterization show a great application of the loop morphology-nature correlation that, during complicated in-situ experiments, the nature of dislocation loops can be easily determined based on their form.

However, it is widely accepted that, in Ni, only interstitial loops can grow into a large size under irradiation while vacancy loops would rather shrink due to the positive bias of dislocation loops for both natures [58–60]. The origin and the thickness-dependency of the growth of vacancy loops in our studies and the previous work [33] has not been theoretically understood. Conventional rate theory based on the dislocation bias model seems insufficient to explain the observed growth of vacancy loops. Conventional rate theory implies that all produced point defects are free and are available for annihilation at sinks. As far as we are concerned, a production bias may be a key point to be taken into account. Woo and Singh suggested a production bias model in which vacancies and interstitials produced in cascades are not equally accessible to different sinks (dislocations and voids) [59]. Here we establish a simple system of rate equations assuming that a fraction $(1-\eta)$ of interstitials form I-clusters within the cascade, so are unavailable to loops while all vacancies remain single PDs :

$$\frac{dC_v}{dt} = G - K_r(D_i + D_v)C_iC_v - k_v^2D_vC_v \qquad \text{Equation (4)}$$

$$\frac{dC_i}{dt} = \eta G - K_r(D_i + D_v)C_iC_v - k_i^2D_iC_i \qquad \text{Equation (5)}$$

where, G is the creation rate by irradiation, $K_r = 4\pi r_c/\Omega$ is the recombination coefficient deduced from Waite's theory [61] with r_c the recombination radius assumed to be the lattice parameter (0.352 nm) and Ω the volume of Ni atom, and k_α^2 is the sink strength for species α. The sink strength is the sum over the different objects (dislocation lines, loops, surfaces) in microstructure. At steady state, we can deduce from Eqs. (4) and (5):

$$k_i^2D_iC_i = k_v^2D_vC_v - G + \eta G \qquad \text{Equation (6)}$$

The growth rate of a vacancy loop reads:

$$v = \frac{\Omega}{b}\left(Z_{l,v}D_vC_v - Z_{l,i}D_iC_i\right) \qquad \text{Equation (7)}$$

Using Eqs. (D3), Equation (6) is written as:

$$v = \frac{\Omega}{b}\left(Z_{l,v} - Z_{l,i}\frac{k_v^2}{k_i^2}\right)D_vC_v + \frac{\Omega}{b}\frac{Z_{l,i}}{k_i^2}G(1-\eta) \qquad \text{Equation (8)}$$

To enable the growth of vacancy loops, it is required that v>0, thus we deduce based on Equation (8) that :

$$1-\eta > -\frac{D_v C_v}{G}\left(k_i^2 \frac{Z_{l,v}}{Z_{l,i}} - k_v^2\right) \qquad \text{Equation (9)}$$

We assume that surfaces are neutral sink for PDs ($Z_{surf,i}=Z_{surf,v}=Z_s$) and the bias factor is the same for dislocation lines and loops ($Z_{line,v}=Z_{loop,v}=Z_v$, $Z_{line,i}=Z_{loop,i}=Z_i$). Thus, the sink strength is written as:

$$k_v^2 = k_{surf,\,v}^2 + k_{loop,v}^2 + k_{line,v}^2 = Z_s k_{surf}^2 + Z_{l,v} k_{loop}^2 + Z_{l,v} k_{line}^2$$

$$k_i^2 \frac{Z_v}{Z_i} = \left(Z_s k_{surf}^2 + Z_{l,i} k_{loop}^2 + Z_{l,i} k_{line}^2\right)\frac{Z_v}{Z_i} = \frac{Z_{l,v} - Z_{l,i}}{Z_{l,i}} k_{surf}^2 + k_v^2 = -B_l k_{surf}^2 + k_v^2$$

Where $k_{surf,\,v}^2$, $k_{loop,v}^2$ and $k_{line,v}^2$ are sink strength depending only on the geometry and density/size of the sink. Finally, Eqs. (D6) is simplified as:

$$1-\eta > \frac{D_v C_v}{G} B_l k_{surf}^2 \qquad \text{Equation (10)}$$

Where D_v is the diffusion coefficient of vacancies, C_v the concentration of vacancies, G production rate of PDs, $B_l = (Z_i - Z_v)/Z_i$ the loop bias factor and k_{surf}^2 the sink strength of free surfaces. At 510°C in a 260 nm thick zone, D_v=4.6x10^{-14} m^2/s deduced from [17], C_v =8x10^{-6}, G=2.7x10^{-4} dpa/s, B_l=0.4 typically for a loop with a radium of 2 nm (Fig. 3.16 in [60]), $k_{surf}^2 = 12/t^2$ where t is the thickness [62], we finally deduce that $1-\eta > 12\%$. These calculations show that if at least ~10% interstitials are "lost", the growth of vacancy loops could be favored. A plausible explanation for this loss of interstitial clusters is that they move in long-distance 1D motion and escape immediately from the production zone, as suggested by [15]. Equation (8) shows that the loop growth rate depends on the sink strength of surfaces therefore the thickness, which is observed in this work.

5. Conclusions

The influence of free surfaces on radiation damage in pure nickel is investigated using in-situ irradiations within the JANNUS-Orsay platform [39] at different temperatures and thin foil thicknesses. Our observations show that:

1) A drastic influence of thickness on the in-situ microstructural evolution and post-irradiated microstructure of Ni in the studied temperature range (400-700°C) is highlighted. This so-called surface effects on loop density and size are firstly attributed to the absorption of point defects by surfaces. Our work clearly demonstrates the existence of a critical thickness, depending on temperature, above which the loop growth rate, loop density and average loop size become independent on the thickness. The critical thickness for 510/450/400°C are respectively 220/100/80 nm.
2) Our vacancy concentration calculations in Ni (based on Foreman formulations [51]) could be an excellent tool to predict an adequate thickness for in-situ irradiations in various materials. They confirm the thickness dependency of the microstructure and the calculated critical thicknesses are in good agreement with those determined in our work.
3) Free surfaces affect the fine distribution of loop Burgers vectors even above the critical thickness. Some perfect loops families with a Burgers vector of **b**=1/2<110> preferentially glide to free surfaces and are absorbed, leading to a heterogeneous distribution of glissile perfect loops. This preferential absorption of perfect loops is related to the orientation of the Burgers vector of the loop and the thin foil normal. The family with the Burgers vectors closer to the foil normal is the most depleted. On the contrary, the distribution of Frank loops,

sessile defects with **b**=1/3<111>, is not affected by free surfaces: they are equally distributed among the four families.

4) For the first time, the migration energy of vacancies in Ni is experimentally determined considering the temperature dependence of the loop-depleted zones. The loop-depleted zones on each side of thin foils are indeed dependent of the irradiation temperature. Their width are about 40 nm at 510°C and 30 nm at 450°C. The fit of our experiment data on the loop depleted zone with the ones extracted from the literature gives a migration energy of 1.20 eV, which is in good agreement with the recognized values in the literature [15,17,54].
5) A rate theory model including production bias term demonstrates that a loss of 10% interstitials, at 510°C, theoretically favors the growth of vacancy loops. It well explains the first observation at 510°C of grown Frank loops and perfect loops all identified as vacancy-type in self-ion irradiated Ni. It contrasts with the conventional rate theory based on the dislocation bias model in which only interstitial loops can grow.

Acknowledgement

The research was supported by the NEEDS program (CNRS-CEA-EDF-ANDRA-AREVA-IRSN-BRGM) and the RMATE project (CEA). Ion beam irradiation was performed at the IJCLab facility: JANNuS-SCALP (IJCLab Univ Paris-Sud / CNRS, Orsay, France); their support is gratefully acknowledged. Irradiation was also supported by the EMIR&A French accelerator network.

Declaration of interests

The authors declare that they have no known competing financial interests or personal relationships that could have appeared to influence the work reported in this paper.

Appendix A. SRIM calculation of radiation damage

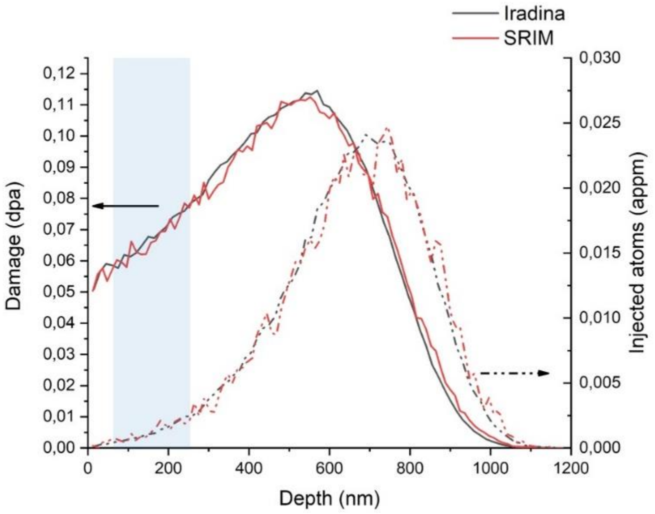

Fig. A. 1 The damage profile of 2 MeV Ni^{2+} ions calculated by SRIM 2013 and IRADINA for a fluence of $9x10^{13}$ ions.cm^{-2} with a displacement threshold energy of 40 eV [25,42,63].

Appendix B. Visibility table for the determination of Burgers vectors

Table B. 1 Visibility table of all families of Frank loops and perfect loops in function of diffraction vectors used for Fig. 6.

Table of visibility (V=visible, I=invisible)									
Zone axes		[011]		[001]				[101]	BV analysis
Possible b	**g**	$\bar{1}\bar{1}1$	$11\bar{1}$	020	$0\bar{2}0$	200	$\bar{2}\bar{2}0$	$\bar{2}02$	
Frank loops	$\pm\frac{1}{3}[111]$	V	V	V	V	V	V	I	Loop A
	$\pm\frac{1}{3}[\bar{1}11]$	V	V	V	V	V	I	V	
	$\pm\frac{1}{3}[1\bar{1}1]$	V	V	V	V	V	I	I	
	$\pm\frac{1}{3}[11\bar{1}]$	V	V	V	V	V	V	V	
Perfect loops	$\pm\frac{1}{2}[110]$	V	V	V	V	V	V	V	
	$\pm\frac{1}{2}[1\bar{1}0]$	I	I	V	V	V	I	V	
	$\pm\frac{1}{2}[101]$	I	I	I	I	V	V	I	
	$\pm\frac{1}{2}[10\bar{1}]$	V	V	I	I	V	V	V	
	$\pm\frac{1}{2}[011]$	I	I	V	V	I	V	V	
	$\pm\frac{1}{2}[01\bar{1}]$	V	V	V	V	I	V	V	Loop B

Appendix C. One-dimensional rate equations of PD concentrations

The concentration profile of point defects along depth direction can be described by one-dimensional steady-state diffusion equations for a given thickness and a given temperature:

$$-D_v \frac{\partial^2 C_v}{\partial z^2} = G - K_r C_v C_i (D_v + D_i) \qquad \text{Equation (3)}$$

$$-D_i \frac{\partial^2 C_i}{\partial z^2} = G - K_r C_v C_i (D_v + D_i) \qquad \text{Equation (4)}$$

Where C_v and C_i are atomic fraction of vacancies and interstitials, D_v and D_i are diffusion coefficients of of vacancies and interstitials, G production rate of point defects in dpa/s, $K_r = 4\pi r_c/\Omega$ the recombination constant (r_c : recombination radius).

Equation (3) and (4) lead to $D_v C_v = D_i C_i$. Considering $D_i \gg D_v$, Equation (3) can be normalized and rewritten as:

$$\frac{\partial^2 Y}{\partial X^2} = \frac{t^2 G}{D_v C_{v,\infty}} (Y^2 - 1) \qquad \text{Equation (5)}$$

Where $Y = C_v / C_{v,\infty}$ with $C_{v,\infty} = \sqrt{G/(K_r D_v)}$ the vacancy concentration in bulk materials without surface effects and $X = z/t$ with t the thickness of specimen.

Equation (5) gives the profile of vacancy concentration. A similar equation was given by Foreman [51]. The form of the profile depends on the thickness, irradiation flux, and the temperature. To solve Equation (5), the diffusion coefficient is calculated by Arrehnius law with parameters as given in [17] and boundary conditions $C_v(z = 0) = 0$ ($C_{v,eq}$ at thermal equilibrium negligible to $C_{v,\infty}$) and $C'_v(z = 0.5) = 0$ (by symmetry).

Reference

[1] S. Ishino, A review of in situ observation of defect production with energetic heavy ions, Journal of Nuclear Materials. 251 (1997) 225–236. https://doi.org/10.1016/S0022-3115(97)00247-X.

[2] K. Urban, Growth of defect clusters in thin nickel foils during electron irradiation (I), Physica Status Solidi (a). 4 (1971) 761–772. https://doi.org/10.1002/pssa.2210040321.

[3] H. Abe, N. Sekimura, Y. Yang, Stability and mobility of defect clusters in copper under displacement cascade conditions, Journal of Nuclear Materials. 323 (2003) 220–228. https://doi.org/10.1016/j.jnucmat.2003.08.006.

[4] D. Chen, K. Murakami, H. Abe, Z. Li, N. Sekimura, Investigation of interactions between defect clusters in stainless steels by in situ irradiation at elevated temperatures, Acta Materialia. 163 (2019) 78–90. https://doi.org/10.1016/j.actamat.2018.10.011.

[5] R.C. Birtcher, M.A. Kirk, K. Furuya, G.R. Lumpkin, M.-O. Ruault, In situ Transmission Electron Microscopy Investigation of Radiation Effects, Journal of Materials Research. 20 (2005) 1654–1683. https://doi.org/10.1557/JMR.2005.0242.

[6] S. Ishino, K. Fukuya, T. Muroga, N. Skinura, H. Kawanishi, In-situ microstructural observation of radiation damage in nickel produced by energetic heavy particles, Journal of Nuclear Materials. 122&123 (1984) 597–601.

[7] M. Kiritani, Microstructure evolution during irradiation, Journal of Nuclear Materials. 216 (1994) 220–264. https://doi.org/10.1016/0022-3115(94)90014-0.

[8] X. Yi, M.L. Jenkins, M.A. Kirk, Z. Zhou, S.G. Roberts, In-situ TEM studies of 150 keV W+ ion irradiated W and W-alloys: Damage production and microstructural evolution, Acta Materialia. 112 (2016) 105–120. https://doi.org/10.1016/j.actamat.2016.03.051.

[9] N. Sekimura, M. Taguchi, S. Ishino, Inhomogeneous microstructural evolution in ion-irradiated austenitic steel, Journal of Nuclear Materials. 155–157 (1988) 828–832. https://doi.org/10.1016/0022-3115(88)90424-2.

[10] S.J. Zinkle, L.L. Snead, Microstructure of copper and nickel irradiated with fission neutrons near 230°C, Journal of Nuclear Materials. 225 (1995) 123–131. https://doi.org/10.1016/0022-3115(94)00670-9.

[11] J.L. Brimhall, B. Mastel, Stability of voids in neutron irradiated nickel, Journal of Nuclear Materials. 33 (1969) 186–194. https://doi.org/10.1016/0022-3115(69)90059-2.

[12] T. Yoshiie, Q. Xu, Y. Satoh, H. Ohkubo, M. Kiritani, The effect of alloying elements on the defect structural evolution in neutron irradiated Ni alloys, Journal of Nuclear Materials. 283–287 (2000) 229–233.

[13] T.M. Robinson, M.L. Jenkins, Heavy-ion irradiation of nickel and nickel alloys, Philosophical Magazine A. 43 (1981) 999–1015. https://doi.org/10.1080/01418618108239507.

[14] I.M. Robertson, J.S. Vetrano, M.A. Kirk, M.L. Jenkins, On the formation of vacancy type dislocation loops from displacement cascades in nickel, Philosophical Magazine A. 63 (1991) 299–318. https://doi.org/10.1080/01418619108204851.

[15] C. Lu, L. Niu, N. Chen, K. Jin, T. Yang, P. Xiu, Y. Zhang, F. Gao, H. Bei, S. Shi, M.-R. He, I.M. Robertson, W.J. Weber, L. Wang, Enhancing radiation tolerance by controlling defect mobility and migration pathways in multicomponent single-phase alloys, Nature Communications. 7 (2016) 13564. https://doi.org/10.1038/ncomms13564.

[16] P. Zhao, Y. Shimomura, Molecular dynamics calculations of properties of the self-interstitials in copper and nickel, Computational Materials Science. 14 (1999) 84–90. https://doi.org/10.1016/S0927-0256(98)00077-9.

[17] J.D. Tucker, R. Najafabadi, T.R. Allen, D. Morgan, Ab initio-based diffusion theory and tracer diffusion in Ni–Cr and Ni–Fe alloys, Journal of Nuclear Materials. 405 (2010) 216–234. https://doi.org/10.1016/j.jnucmat.2010.08.003.

[18] D.I.R. Norris, Dislocation loop growth in an electron irradiated thin foil, Philosophical Magazine. 22 (1970) 1273–1278. https://doi.org/10.1080/14786437008226935.

[19] M.H. Yoo, J.O. Stiegler, Growth kinetics and ‘preference factor’ of Frank loops in nickel during electron irradiation, Philosophical Magazine. 36 (1977) 1305–1315. https://doi.org/10.1080/14786437708238518.

[20] J.E. Harbottle, D.I.R. Norris, High voltage electron microscope studies of void nucleation in nickel, Journal of Microscopy. 97 (1973) 129–138. https://doi.org/10.1111/j.1365-2818.1973.tb03767.x.

[21] K.M. Miller, Interstitial loop growth in HVEM-irradiated nickel foils, Journal of Nuclear Materials. 115 (1983) 216–222. https://doi.org/10.1016/0022-3115(83)90313-6.

[22] M. Kiritani, N. Yoshida, H. Takata, Y. Maehara, Growth of Interstitial Type Dislocation Loops and Vacancy Mobility in Electron Irradiated Metals, Journal of

the Physical Society of Japan. 38 (1975) 1677–1686. https://doi.org/10.1143/JPSJ.38.1677.

[23] A.D. Brailsford, R. Bullough, The rate theory of swelling due to void growth in irradiated metals, Journal of Nuclear Materials. 44 (1972) 121–135. https://doi.org/10.1016/0022-3115(72)90091-8.

[24] K. Urban, M. Wilkens, Growth of defect clusters in thin nickel foils during electron irradiation. II. Temperature dependence of the growth rate of interstitial loops, Physica Status Solidi (a). 6 (1971) 173–185.

[25] G.S. Was, Fundamentals of Radiation Materials Science: Metals and Alloys, Springer, 2016.

[26] K. Nordlund, A.E. Sand, F. Granberg, S.J. Zinkle, R. Stoller, R.S. Averback, T. Suzudo, L. Malerba, F. Banhart, W.J. Weber, Primary radiation damage in materials, Report Prepared by the OECD/NEA Working Party on Multiscale Modelling of Fuels and Structural Materials for Nuclear Systems, Expert Group on Primary Radiation Damage Nuclear Science NEA/NSC/DOC. 9 (2015).

[27] H. Sakaida, N. Sekimura, S. Ishino, In-situ observation of cascade damage in nickel and copper under heavy ion irradiation, Journal of Nuclear Materials. 179–181 (1991) 928–930. https://doi.org/10.1016/0022-3115(91)90241-X.

[28] N. Sekimura, S. Ishino, The effect of titanium addition on microstructural evolution in austenitic steel irradiated with fast neutrons in FFTF, Journal of Nuclear Materials. 179–181 (1991) 542–545. https://doi.org/10.1016/0022-3115(91)90145-W.

[29] K. Niwase, T. Ezawa, T. Tanabe, M. Kiritani, F.E. Fujita, Dislocation loops and their depth profiles in He+ and D+ ion irradiated nickel, Journal of Nuclear Materials. 203 (1993) 56–66. https://doi.org/10.1016/0022-3115(93)90430-7.

[30] L.E. Seitzman, L.M. Wang, G.L. Kulcinski, R.A. Dodd, The effect of oxygen on void stability in nickel and austenitic steel, Journal of Nuclear Materials. 141–143 (1986) 738–742. https://doi.org/10.1016/0022-3115(86)90083-8.

[31] A.D. Brailsford, L.K. Mansur, Effect of self-ion injection in simulation studies of void swelling, Journal of Nuclear Materials. 71 (1977) 110–116. https://doi.org/10.1016/0022-3115(77)90194-5.

[32] F.A. Garner, Impact of the injected interstitial on the correlation of charged particle and neutron-induced radiation damage, Journal of Nuclear Materials. 117 (1983) 177–197. https://doi.org/10.1016/0022-3115(83)90023-5.

[33] K. Ma, B. Décamps, A. Fraczkiewicz, F. Prima, M. Loyer-Prost, Drastic influence of micro-alloying on Frank loop nature in Ni and Ni-based model alloys, Materials Research Letters. 8 (2020) 201–207. https://doi.org/10.1080/21663831.2020.1741042.

[34] B.C. MASTERS, Dislocation Loops in Irradiated Iron, Nature. 200 (1963) 254–254. https://doi.org/10.1038/200254a0.

[35] W. Wu, R. Schäublin, The elasticity of the ½ a0 and a0 dislocation loop in α-Fe thin foil, Journal of Nuclear Materials. 510 (2018) 61–69. https://doi.org/10.1016/j.jnucmat.2018.07.057.

[36] J. Malaplate, B. Michaut, A. Renault-Laborne, T. Jourdan, F. Dalle, F. Sefta, B. Décamps, Investigation of ion irradiation defects microstructure and cavity swelling evolution in austenitic steels representative of PWR internals, in: Thermec’2018, Thermec’2018, Paris, 2018.

[37] D. Xu, B.D. Wirth, M. Li, M.A. Kirk, Combining in situ transmission electron microscopy irradiation experiments with cluster dynamics modeling to study

nanoscale defect agglomeration in structural metals, Acta Materialia. 60 (2012) 4286–4302. https://doi.org/10.1016/j.actamat.2012.03.055.

[38] M. Li, M.A. Kirk, P.M. Baldo, D. Xu, B.D. Wirth, Study of defect evolution by TEM with in situ ion irradiation and coordinated modeling, Philosophical Magazine. 92 (2012) 2048–2078. https://doi.org/10.1080/14786435.2012.662601.

[39] C.-O. Bacri, C. Bachelet, C. Baumier, J. Bourçois, L. Delbecq, D. Ledu, N. Pauwels, S. Picard, S. Renouf, C. Tanguy, SCALP, a platform dedicated to material modifications and characterization under ion beam, Nuclear Instruments and Methods in Physics Research Section B: Beam Interactions with Materials and Atoms. 406 (2017) 48–52. https://doi.org/10.1016/j.nimb.2017.03.036.

[40] M.H. Loretto, R.E. Smallman, Defect analysis in electron microscopy, Chapman and Hall, New York, 1975.

[41] J.F. Ziegler, Nuclear instruments and methods in physics research section B: Beam interactions with materials and atoms, SRIM-2003. 219 (2004) 1027–1036.

[42] R.E. Stoller, M.B. Toloczko, G.S. Was, A.G. Certain, S. Dwaraknath, F.A. Garner, On the use of SRIM for computing radiation damage exposure, Nuclear Instruments and Methods in Physics Research Section B: Beam Interactions with Materials and Atoms. 310 (2013) 75–80. https://doi.org/10.1016/j.nimb.2013.05.008.

[43] J.-P. Crocombette, C. Van Wambeke, Quick calculation of damage for ion irradiation: implementation in Iradina and comparisons to SRIM, EPJ Nuclear Sci. Technol. 5 (2019) 7. https://doi.org/10.1051/epjn/2019003.

[44] David B. Williams, C. Barry Carter, Transmission Electron Microscopy: A Textbook for Materials Science, Springer US, n.d.

[45] P.A. Stadelmann, JEMS-EMS java version, CIME-EPFL, Lausanne, Switzerland. (2004).

[46] A. Prokhodtseva, B. Décamps, A. Ramar, R. Schäublin, Impact of He and Cr on defect accumulation in ion-irradiated ultrahigh-purity Fe(Cr) alloys, Acta Materialia. 61 (2013) 6958–6971. https://doi.org/10.1016/j.actamat.2013.08.007.

[47] P.B. Hirsch, Electron microscopy of thin crystals, Plenum Press, 1967.

[48] M.L. Jenkins, Characterisation of radiation-damage microstructures by TEM, Journal of Nuclear Materials. 216 (1994) 124–156. https://doi.org/10.1016/0022-3115(94)90010-8.

[49] J.L. Brimhall, E.P. Simonen, Effect of helium on void formation in nickel, Journal of Nuclear Materials. 68 (1977) 235–243.

[50] B.A. Bilby, R. Bullough, S. Edwin, Continuous distributions of dislocations: a new application of the methods of non-Riemannian geometry, Proc. R. Soc. Lond. A. 231 (1955) 263–273. https://doi.org/10.1098/rspa.1955.0171.

[51] A.J.E. Foreman, The diffusion of point defects to the foil surface during irradiation damage experiments in the high voltage electron microscope, Radiation Effects. 14 (1972) 175–179. https://doi.org/10.1080/00337577208231197.

[52] M. Rühle, F. Häussermann, M. Rapp, Transmission Electron Microscopy of Point-Defect Clusters in Neutron-Irradiated Metals. I. Copper, Physica Status Solidi (b). 39 (1970) 609–620.

[53] S. Hasanzadeh, R. Schäublin, B. Décamps, V. Rousson, E. Autissier, M.F. Barthe, C. Hébert, Three-dimensional scanning transmission electron microscopy of dislocation loops in tungsten, Micron. 113 (2018) 24–33. https://doi.org/10.1016/j.micron.2018.05.010.

[54] G.M. Poletaev, M.D. Starostenkov, Contributions of different mechanisms of self-diffusion in face-centered cubic metals under equilibrium conditions, Physics of the Solid State. 52 (2010) 1146–1154. https://doi.org/10.1134/S1063783410060065.

[55] M.I. Baskes, C.L. Bisson, W.D. Wilson, Calculations of the trapping and migration of vacancies and nickel self-interstitials in the presence of rare gases and dislocations, Journal of Nuclear Materials. 83 (1979) 139–146. https://doi.org/10.1016/0022-3115(79)90599-3.

[56] D. Hull, D.J. Bacon, Introduction to dislocations, 5. ed, Elsevier/Butterworth-Heinemann, Amsterdam, 2011.

[57] M.J. Makin, Electron displacement damage in copper and aluminium in a high voltage electron microscope, The Philosophical Magazine: A Journal of Theoretical Experimental and Applied Physics. 18 (1968) 637–653. https://doi.org/10.1080/14786436808227466.

[58] R. Bullough, M.H. Wood, D.W. Wells, J.R. Willis, THE INTERACTION ENERGY BETWEEN INTERSTITIAL ATOMS AND DISLOCATIONS AND ITS RELEVANCE TO IRRADIATION DAMAGE PROCESSES, in: M.F. ASHBY, R. BULLOUGH, C.S. HARTLEY, J.P. HIRTH (Eds.), Dislocation Modelling of Physical Systems, Pergamon, 1981: pp. 116–141. https://doi.org/10.1016/B978-0-08-026724-1.50017-0.

[59] C.H. Woo, B.N. Singh, Production bias due to clustering of point defects in irradiation-induced cascades, Philosophical Magazine A. 65 (1992) 889–912. https://doi.org/10.1080/01418619208205596.

[60] D. Carpentier, Simulation de la cinétique d'absorption des défauts ponctuels par les dislocations et amas de défauts, Ph.D. thesis, Université Paris-Saclay, 2018. https://pastel.archives-ouvertes.fr/tel-01915303/document.

[61] T.R. Waite, Theoretical Treatment of the Kinetics of Diffusion-Limited Reactions, Phys. Rev. 107 (1957) 463–470. https://doi.org/10.1103/PhysRev.107.463.

[62] F.A. Nichols, On the estimation of sink-absorption terms in reaction-rate-theory analysis of radiation damage, Journal of Nuclear Materials. 75 (1978) 32–41. https://doi.org/10.1016/0022-3115(78)90026-0.

[63] J.-P. Crocombette, L. Van Brutzel, D. Simeone, L. Luneville, Molecular dynamics simulations of high energy cascade in ordered alloys: Defect production and subcascade division, Journal of Nuclear Materials. 474 (2016) 134–142. https://doi.org/10.1016/j.jnucmat.2016.03.020.